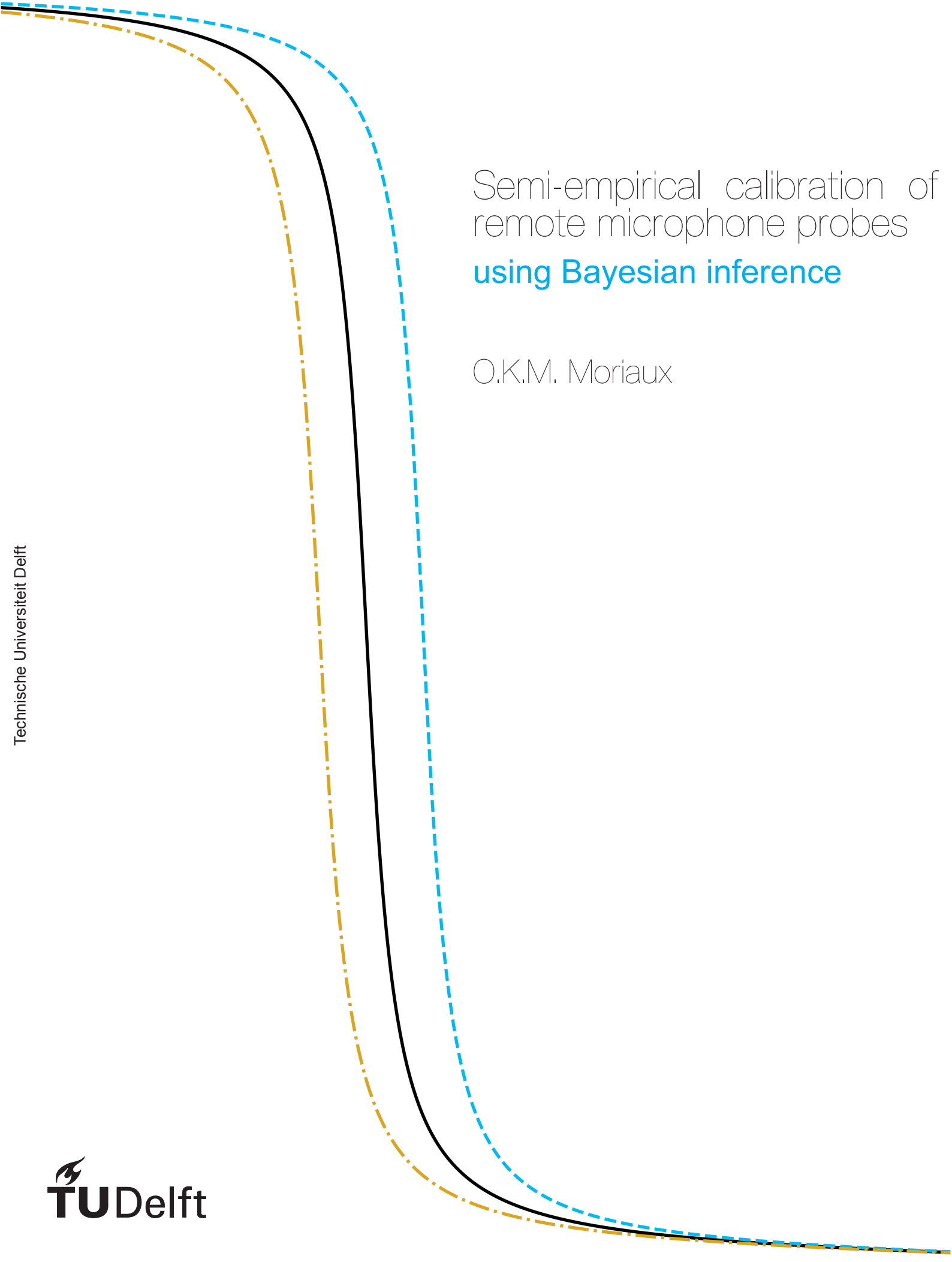

Semi-empirical calibration of remote microphone probes using Bayesian inference

O.K.M. Moriaux

Technische Universiteit Delft

TU Delft

Semi-empirical calibration of remote microphone probes

using Bayesian inference

by

O.K.M. Moriaux

to obtain the degree of Master of Science
at the Delft University of Technology,
to be defended publicly on Friday February 17, 2023 at 13:30.

Student number: 4478290
Project duration: March 1, 2021 – February 17, 2023
Thesis committee:

Dr. D. Ragni,	TU Delft, Chairperson
Dr. R. Zamponi,	TU Delft, Supervisor
Dr. T. Sinnige,	TU Delft, Examiner
Prof. C. Schram,	von Karman Institute for Fluid Dynamics, Supervisor

TU Delft

Preface

This document marks the final milestone in what feels like a long journey. During such moments it is only natural to be grateful for those that helped us along the way.

First and foremost, to my parents, I am forever grateful. Your eternal guidance and support have in large part brought me to this point.

Second, at the Delft University of Technology I have found a community of passionate lecturers and colleagues. The friendships forged with several of these colleagues, during late nights working on project work, remain of great value to me. ”COZ we can”.

Third, the community of technicians, researchers, and academici at the von Karman Institute for Fluid Dynamics have taught me the art of experimental aerodynamics in the finest detail with great patience.

Finally, my gratitude goes out to everyone involved in the supervision of my Master thesis. My deepest gratitude goes towards my daily supervisor Dr. Riccardo Zamponi for his endless dedication in helping me get the most out of my thesis, for all the opportunities that he has provided to me, and for teaching me the tools that I will need in the next stages of my career. Thank you Prof. Christophe Schram. Your contagious enthusiasm toward this project, and your assistance in understanding the physics of microphone probes are greatly appreciated. Thank you to Dr. Daniele Ragni for your valuable feedback, which included redirecting the thesis project from the initial topic to the one presented here.

O.K.M. Moriaux
Sint-Genesius-Rode, January 2023

Contents

1

Introduction

Unsteady wall-pressure measurements are acquired in a wide range of aerodynamic experimental campaigns. Surface pressures determine steady and unsteady forces that act upon a body submerged in a flow, e.g., the unsteady aerodynamic response of airfoils to unsteady inflow conditions [1]. An array of unsteady surface-pressure measurement locations can provide crucial information on the flow over a surface and its stability, e.g., separation bubbles on airfoils [2] or in rocket nozzles during start-up at sea level [3]. Furthermore, these measurements can be linked to turbulent structures within the boundary layer [4, 5], and they are one of the primary sources of noise production of bodies immersed in a flow [6, 7].

Because surface pressures provide such crucial information to the experimentalist, a wide array of measurement techniques exist to acquire them, from U-tube manometers to pressure-sensitive paints. Nevertheless, due to their fast response and accuracy, the conventional apparatuses used for unsteady-pressure measurements are typically microphones. These can be either flush-mounted on the surface or mounted remotely inside a cavity connected to the surface through a system of tubes or a pinhole.

Remote microphone probes (RMPs), including pinhole probes, tend to be preferred over flush-mounted probes when acquiring unsteady wall-pressure fluctuations. With RMPs, the bulk of the probe can be moved away from any space-constraining geometry, and its sensing area can be decreased. A smaller probe can be used in a wider array of geometries with minimal flow interference. And the sensing area of the probe impacts the averaging of acquired high-frequency turbulent pressure fluctuations with wavelengths of similar size to or larger than the sensing area [8]. The method of Corcos [8] can be used to correct several derived quantities of the pressure fluctuations for this averaging effect for specific inflow conditions. By decreasing the sensing area, the correction factor can be reduced, decreasing, in turn, the possible inaccuracies introduced by the assumptions of Corcos' method. In addition, reducing their dimensions enables the sensing areas to be positioned in a tighter grid, which improves wall-pressure-derived flow quantities such as correlation length and convection speed.

Flush mounting the transducer allows direct measurement of the pressure in the region of interest. In contrast, pneumatic systems built from capillary tubes, junctions, and volumes result in the viscous attenuation and internal reflections of the incoming pressure waves. Hence, the pressure fluctuations measured by the remote transducer are altered from the fluctuations at the RMP orifice in the region of interest. This frequency-dependent amplification and phase delay of pressure fluctuations is defined as the transfer function (TF) of the system. The most straightforward RMP geometry, i.e., a pinhole probe, acts as a Helmholtz resonator. The TF of an example pinhole probe is presented in fig. 1.1. As can be seen, low-frequency pressure fluctuations will tend to remain unaffected by the dynamics of the RMP. However, at higher frequencies, e.g., above ca. $100\,\mathrm{Hz}$ for fig. 1.1, attenuation from viscosity in the lines and resonance from the cavity and lines affect the incoming pressure fluctuations. In eq. (1.1), simple equations that can be used to estimate resonant frequencies are presented and compared to the theoretical TF of a probe in fig. 1.1.

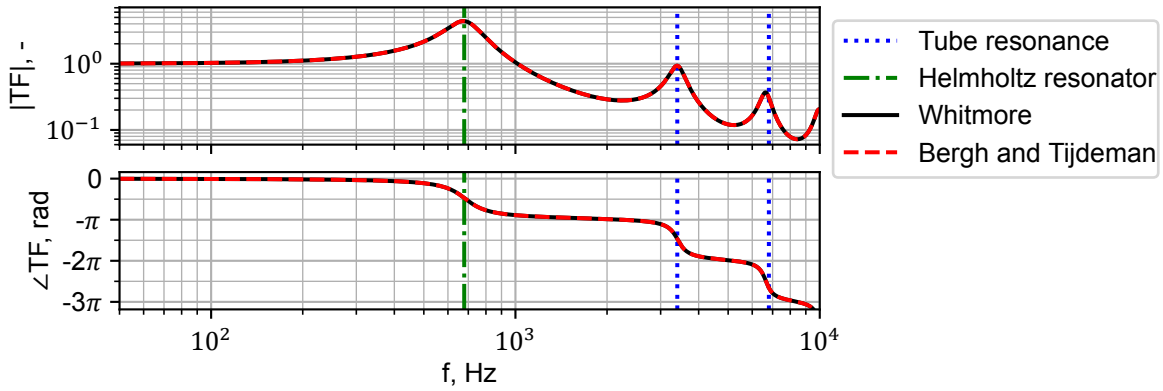

Figure 1.1: Pinhole TF, from the inlet to the cavity, modeled with the theoretical framework of Bergh and Tijdeman [9] and Whitmore [10]. Resonant frequencies of half wavelength and Helmholtz resonator are overlayed following eq. (1.1). Pinhole parameters: $(L, R, V) = (50\,\text{mm}, 0.5\,\text{mm}, 40\,\text{mm}^3)$, $c_0 = 340.26\,\text{m}\,\text{s}^{-1}$, $\nu = 1.46\,\text{m}^2\,\text{s}^{-1}$.

$$\text{Helmholtz for cavity-backed lines: } f_c = \frac{c}{2\pi}\sqrt{\frac{\pi R^2}{V_v L}} = \frac{c}{2L}\sqrt{\frac{V_t}{V_v}}$$
$$\text{Open-ended tube resonance: } f_{r,t} = \frac{c}{2L}\cdot n \quad \text{with } n \in \mathbb{N}_1 \tag{1.1}$$

Here, f is frequency, c is the speed of sound, L and R are the length and radius of the pinhole, $V_t = L\pi R^2$ is the tube volume of the pinhole, and V_v is the cavity volume behind the pinhole tube.

When acquiring unsteady-pressure measurements with a RMP probe, the goal is to have the measurement reflect the physics of the pressure fluctuations of the flow at the inlet of the probe, unaffected by the specific TF of the measurement instrument. Hence, for accurate unsteady-pressure measurements, the TF of the RMP needs to be estimated so that the impact of the probe on the measurements can be subtracted from them. In other words, the inverse of the probe TF needs to be applied to the measurements. Frequencies at which the probe has a strong attenuation of the incoming pressure signal are amplified considerably by the inverse TF. Therefore, even a small error in the TF amplitude in these frequency bands leads to a considerable error in the inverse TF and, thus, the TF-corrected measurement data. In summary, the accuracy of TF estimation is critical.

The TF of the probe can be estimated either through an analytic or empirical calibration method. By simplifying the Navier-Stokes and energy equations, these analytic methods can provide closed-form solutions for the TF of the probe given several probe geometries and flow properties as parameters [9, 10]. An advantage of these analytic models is that they provide the theoretically correct TF without any measurement error. In addition, expansions to these models are used to correct the TF for changes in flow conditions that impact the TF of the probe [11]. However, these models only provide accurate results as long as their underlying assumptions are valid, and exact knowledge of the input parameters, e.g., calibrator-tube length and pinhole-cavity volumes, to the models is needed to achieve an accurate TF.

In contrast, empirical frequency-domain dynamic calibration methods [12, p.70] rely on relating the frequency response of the probe being calibrated to that of a reference flush-mounted probe when both are subjected to the same sound source. These methods are based on little-to-none assumptions and do not require knowledge about the exact shape of the probe being calibrated or the flow conditions. In addition, with empirical calibration methods, the acquired TF includes both the TF of the pneumatic system linking the transducer to the surface and that of the transducer itself. Analytic models can only account for the first. For these reasons, analytic models tend to be used as a tool with which to design RMPs with a favorable TF, while empirical calibration methods, e.g., plane-wave calibrators, are the convention for calibrating pressure probes. However, two major problems can be found with the empirical calibration process: (i) the calibration conditions often do not reflect the conditions when the RMP is in use, e.g., with the probe immersed in a grazing flow or high-temperature environments, and (ii) the calibrator equipment itself is a tube-volume system that can introduce resonant frequencies into the final TF.

The TF of a probe depends on several properties of the flow, such as its mean temperature and

pressure. When acquiring the calibration of a probe empirically, the TF is that of the probe at the temperature and pressure at which it is subject during the calibration. During the measurement campaign, between RMP calibrations, the atmospheric conditions can fluctuate, impacting the response of the probe. However, these measurements are corrected with a TF linked to the probe at different conditions, inducing errors in the calibrated measurements. Even larger differences in measurement and calibration conditions occur in high-temperature experiments [13]. Similarly, Tijdeman and Bergh [11] have found that flow grazing over the orifice of a pressure probe acts as a membrane that impedes the free in-and-out movement of pressure waves, changing the TF of the probe. Not accounting for this effect could induce errors in the calibrated measurements, especially for high Mach-number flows.

The problem of calibrator-induced resonance in the final calibration of the probe is termed spurious resonance, as it is not related to the actual response of the probe but to the calibrator tube-cavity geometry. The conventional calibration approach with a plane-wave calibrator uses two or more calibration steps, see fig. 1.2. To link the frequency response of the RMP to that of the flush-mounted reference microphone, it is first related to an intermediate microphone in the calibrator. The TF of the calibrator is supposed to fully cancel out when the two calibration steps are combined, see eq. (1.2). In this equation, $S_{x,y}$ represents the cross-power-spectral density between signal x and y, and $\mathscr{F}$ represents the Fourier-transform operator. For this to be theoretically correct and able to link both calibration steps together with the calibrator microphone, the same pressure field needs to be present in both calibration steps. This is one of the few assumptions of the empirical calibration approach, which, according to Van de Wyer et al. [14], often does not hold. The reason behind the difference in pressure fields comes from the unequal sensing areas of the microphone probes: on the one hand, there is a 6.35 mm (1/4 inch) flush-mounted microphone that serves as a reference microphone for the calibration, while, on the other hand, there is a RMP, which has a hole diameter in the order of 0.1 mm to 1 mm. The different sensing area in the two cases results in a different impedance of the lower wall of the calibrator for both measurement steps. For the same speaker input, the internal pressure field of the calibrator, as well as the boundary conditions of the system, differs. As a result, the resonance of the calibrator-tube sections will have different strengths, in both amplitude and phase, for each calibration step. Consequently, these calibrator-induced resonant frequencies will no longer cancel out when combining the TFs of the two calibration steps.

$$TF_{\text{RMP}\rightarrow\text{ref.}}(f) = \frac{S_{\text{ref., RMP}}(f)}{S_{\text{RMP, RMP}}(f)} = \frac{\mathscr{F}\left[p'_{\text{ref.}}\right]}{\mathscr{F}\left[p'_{\text{RMP}}\right]} = \underbrace{\frac{\mathscr{F}\left[p'_{\text{ref.}}\right]}{\cancel{\mathscr{F}\left[p'_{\text{cal}}\right]}}}_{TF_{\text{cal}\rightarrow\text{ref.}}} \underbrace{\frac{\cancel{\mathscr{F}\left[p'_{\text{cal}}\right]}}{\mathscr{F}\left[p'_{\text{RMP}}\right]}}_{TF_{\text{RMP}\rightarrow\text{cal}}} \tag{1.2}$$

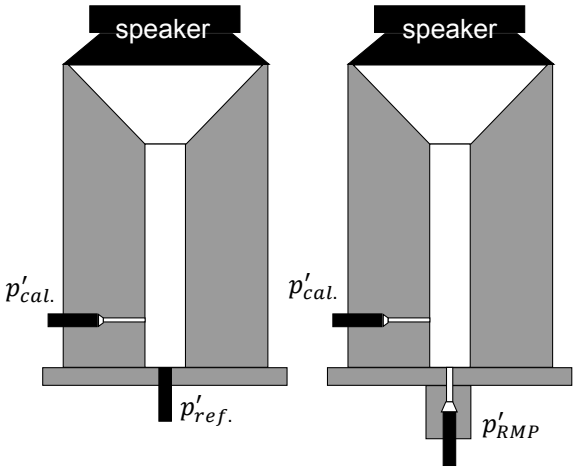

Figure 1.2: Two-step calibration method with a plane-wave tube. Step 1: TF linking the **ref**erence microphone with the **cal**ibrator microphone. Step 2: TF linking the **cal**ibrator microphone with the microphone being calibrated, e.g., **RMP**.

One might think that the spurious resonance phenomena described above result in a small, negligible error, but this is not the case. In fig. 1.3, the SPL of the microphones is compared over both calibration steps. The most apparent difference in the pressure fields occurs at around 1 kHz. The

pressure field at the calibrator side-branch microphone also differs at 3 kHz and 9 kHz, which correspond to the first and third modes of the calibrator-tube section, respectively.

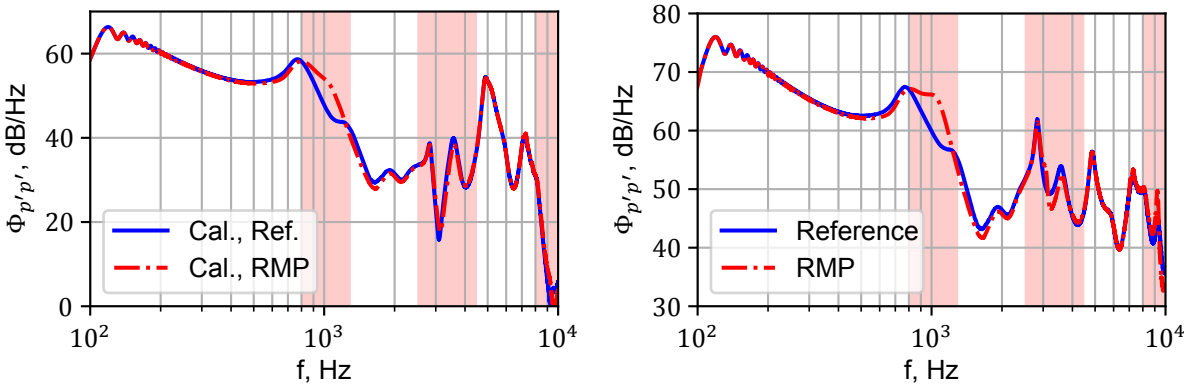

(a) Comparison between the calibrator microphone when the reference and RMP microphones are mounted.

(b) Comparison between the 'reference' flush-mounted- B&K and a RMP microphone. RMP signal calibrated with TF.

Figure 1.3: Sound pressure level comparison between microphones of two different plane-wave calibration steps. Red-shaded regions indicate regions including spurious resonance in the final TF.

Currently, TFs affected by spurious resonance tend to be processed manually to minimize their effect on any pressure measurements corrected with the TF. Van de Wyer et al. [14] combines TFs from different signals and smooths the result, while [15] uses multiple calibrations to determine the resonant frequencies and uses theory to determine the correct attenuation. These manual methods are strongly operator-dependent for the choice of which resonance to remove and how to replace the affected frequency bands. Therefore, the expected TF of the RMP must be well understood in order not to overlook spurious resonance, or introduce additional errors in the calibration.

While the aforementioned analytic models can aid in understanding the expected TF, it is still a heavily operator-reliant method. Instead, the idea is to develop a novel calibration method that combines the synergistic strengths of both empirical and analytic calibration methods. By fitting an analytic TF model onto empirical calibration data: spurious resonance that is not physically possible for the considered probe and model physics is removed, but no exact knowledge is required of the RMP parameters as they are inferred from the fit with the calibration data. The flow conditions of this model TF can then also be easily changed to better reflect the TF of the probe during measurement, resolving the second issue with the current empirical calibration approach. Alternatively, the parameter values found in the fit can be used for corrective models for the effect of grazing flow [5, 11], sensing area [8] etc.

A functioning 'semi-empirical' calibration method can be developed by simply iteratively changing the parameter values randomly and accepting these new parameter samples based on the quality of the model fit, e.g., quantified by the cumulative difference between the data and model. Such a method uses a single information source: the empirical calibration data. A better-suited method for fitting models to data, with possible measurement errors, is Bayesian inference (BI). This is because the BI method uses information from two primary sources: the empirical calibration data and the prior knowledge of the (pressure measurement) system. It aims to minimize the difference between the measurements and the model while also considering the probability of the parameter values needed for that fit.

Bayesian inference comes from Bayesian statistics, which has a different way of looking at the concept of probability than Frequentist statistics. In short, the probability of a certain measurement outcome can only be defined by repeatedly performing said measurement. The variance in the measurements is linked to the randomness of the system, according to the Frequentist way of thinking about probability. In contrast, the Bayesian concept of probability sees the variance of the measurement results as a product of our lack of system knowledge. The probability of the measurements is used to quantify the uncertainty about the system and its input parameters, from which part of this variance could stem. This uncertainty can be defined without the need for repeated measurements. And by repeatedly measuring, a better understanding of the possible variance of results is gained, and the bounds of uncertainty can be shrunken.

An immediate benefit of the BI approach is achieved for systems with parameters that provide overlapping effects. An equally good fit of the model can be provided for different parameter combinations. No unique solution would emerge from the 'simple-fitting' method. The BI accounts for the probability of the parameter values and will prioritize combinations where each separate parameter is within a realistic range. As such, the fit of BI may be less close to the data than the 'simple-fitting' method, but the parameters, and thus the TF, are more likely to be physically correct. New, less probable parameter values will be accepted only when the data show a large enough difference in fit quality. Therefore, spurious resonance in the calibration data being fit will not as easily pull the fitting solution to unrealistic parameter values. Due to these capabilities of BI, it has been applied to many problems, from regularization in MaxEnt image processing [16] and beamforming [17] to enhancing PIV data [18].

The aim of this dissertation is thus to develop a novel calibration method with (i) reduced operator dependence on the final TF that (ii) uses fluid-dynamical theory to determine which resonance should be removed from the TF. Hence, the main research objective is to:

> "Remove calibrator-induced spurious resonant peaks from the transfer functions of microphone probes acquired with an empirical plane-wave-tube calibration method by coupling the calibration data with analytic models for the frequency response of pneumatic systems."

As mentioned, the proposed method can be used to address the discrepancy of conditions between calibration and measurements. The wall-pressure spectrum (WPS) model of Goody [19] is used to provide a quantitative comparison between the current empirical calibration method and the proposed method. Lastly, this new calibration approach has the potential to provide accurate calibrations in challenging conditions due to the physics-driven processing. The following *sub-objectives* form the requirements for these planned features.

1. Reduce the deviation between the measured WPS to the spectra predicted through Goody's model at $M = 0.1$ by $10\,\%$, by accounting for the effect of grazing flow in the calibration of the RMP.
2. Use a frequency response model for pneumatic systems to correct for isentropic changes in mean pressure and temperature between the time of calibration and the time of data acquisition with a RMP.
3. Use the frequency response model fitting to reconstruct frequency bands of the TF that are affected by improper sealing of the calibrator on a porous surface.
4. Provide a single-step calibration method with the plane-wave calibrator by removing the calibrator influence from the TF fit of the complete calibrator and RMP system.

In the pursuit of the development of the new method, several *research questions* can be formulated and linked to the objectives.

1. How is the spurious resonance affected by the calibrator geometry?
2. How is the TF of a semi-infinite waveguide probe and pinhole affected by its geometry?
3. How is the TF fit affected by the model assumptions?
4. How can the calibration data be preprocessed to improve the resulting fit from the method?
5. How strongly does the uncertainty estimate for the frequency response of the RMP provided by the semi-empirical calibration method depend on the input of the user?
   (a) How dependent is the uncertainty estimate on the PDF of the priors?
   (b) How dependent is the uncertainty estimate on the estimated measurement error variance?
6. How is the grazing flow effect influenced by the parameters of a RMP?
7. How is the modeled effect of a drift in temperature affected by the linearization of the model?
8. What error in the WPS is made when using the method to correct for a 10 K change in temperature with respect to recalibrating the RMP?

9. How are the measured amplitude and phase of a RMP TF affected when calibrated in-situ?
10. What calibration methods are available for the low-to-mid frequency range that do not depend on a sealed calibration environment?
11. What additional data processing is required to achieve an accurate in-situ calibration of a RMP in a porous liner with the semi-empirical calibration method?
12. How well can the W model approximate the TF of the closed-off speaker-driven calibrator compared to more complex models?

The proposed method relies on two elements, both presented in chapter 2: an analytic model for the frequency response of pneumatic systems and a method to couple the model to the data. In chapter 3, the details regarding the implementation of the method and the acquisition of a new experimental campaign for its application are presented. In chapter 4, the different datasets to which the method is applied are discussed. Using these examples, the strengths and limitations of the proposed approach are shown. Finally, in chapter 5, the main findings of this dissertation are summarized.

2

Theory: Description of the semi-empirical calibration method

The theory at the basis of the proposed semi-empirical calibration method is summarized in this section. First, the physics of the propagation of acoustic waves through tubes are analyzed thoroughly. Second, the analytical model of Whitmore [10], used to describe the TF of a pinhole probe with varying parameters of the tubes, is mentioned in section 2.1. Lastly, the statistical framework of the Bayesian inference (BI) and the employed Markov chain Monte Carlo (McMC) method, which are employed to couple the aforementioned theoretical model to the calibration data, are explained in section 2.2.

2.1. Tube-transducer model

The TF of a RMP can be modeled through simplified governing equations for the internal flow field. This approach requires exact knowledge of the geometry of the system and the properties of the internal flow. The effective dimensions can be different due to production or assembly inaccuracies, e.g., additional cavity volume created by the microphone-membrane protection grid. Additionally, these models do not account for the gain of the acquisition system or the TF of the microphone. For a complete TF of the real-world system, an empirical part of the calibration procedure is still required.

Many analytical frequency-response models for pneumatic systems exist [9, 10, 20–24]. A common approach is to model the system as sections of tube-transducer subsystems, see fig. 2.1 and fig. 2.2, each of them being a separate continuum with inflow and outflow boundaries that are dependent on the neighboring sub-systems. This lends itself to a modular method, which allows for describing any RMP topology. These methods not only offer a satisfactory way to model a TF of an existing system but also a valid way to design a RMP.

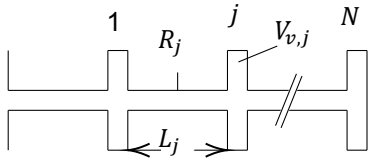

Figure 2.1: Tube-transducer elements in series.

In the method proposed in this research, the Whitmore [10] (W) model is chosen since an often considered geometry for highly accurate measurement systems is that of a semi-infinite waveguide probe, i.e., a branching tube-transducer system constituted of a primary channel with anechoic termination and a side branch containing the transducer. As mentioned by Whitmore [10], this model effectively works in a similar way as Kirchhoff's laws and builds an equivalent serial tube-transducer system from the parallel topology using eq. (2.1), as also illustrated in fig. 2.2. Equation (2.1) can be rewritten using the parameter definitions employed by [9]. The model considers the effect of tube-transducer serial

subsystems and parallel junctions on a prior tube-transducer '$j-1$', closer to the inlet, by using complex effective volumes V_{e_j} for the transducer cavity. The i subscript denotes the index of the parallel branches connected to the junction being considered, while the j subscript is kept for the serial subsystems. Both serial and parallel nodes use the same equation for the effective volume, as a serial node is simply a parallel node with a single branch.

$$\frac{p_j}{p_{j-1}} = \left[\cosh\langle\phi_j L_j\rangle + \frac{V_{e_j}}{V_{t_j}}\phi_j L_j \sinh\langle\phi_j L_j\rangle\right]^{-1} \quad \text{with } V_{e_j} = V_{v_j} + \sum_{i=1}^{N} V_{v_j}\Phi_{i,j} \quad V_{e_N} = V_{v_N}$$

$$V_{v_j}\Phi_{i,j} = V_{e_i}\left(\frac{c_j}{c_i}\right)^2 \frac{\cosh\langle\phi_i L_i\rangle + \sinh\langle\phi_i L_i\rangle / \left(\phi_i L_i V_{e_i}/V_{t_i}\right)}{\cosh\langle\phi_i L_i\rangle + \sinh\langle\phi_i L_i\rangle \cdot \left(\phi_i L_i V_{e_i}/V_{t_i}\right)} \quad \text{For serial node : } i = j+1 \tag{2.1}$$

$$\phi_j = \frac{\omega}{c_j}\sqrt{\frac{J_0\langle\alpha_j\rangle}{J_2\langle\alpha_j\rangle}}\sqrt{\frac{\gamma}{n_j}} \qquad \alpha_j = i^{3/2}R_j\sqrt{\frac{\rho_{s_j}\omega}{\mu_j}} \qquad n_j = \left[1 + \frac{\gamma-1}{\gamma}\frac{J_2\langle\alpha_j\sqrt{Pr}\rangle}{J_0\langle\alpha_j\sqrt{Pr}\rangle}\right]^{-1}$$

ϕ_j is the wave propagation factor, ω is the radial frequency, J_k is the Bessel function of the first kind of order k, α_j is the shear wavenumber, γ is the ratio of specific heats, n_j is the polytropic exponent, ρ_{s_j} is the mean density in the tube, μ_j is the dynamic viscosity in the tube, Pr is the Prandtl number, and $\Phi_{i,j}$ is the branch complex impedance.

In the example presented in fig. 2.2, the TF from the inlet of the system to a transducer situated in the cavity of element $(1,0)$ is computed in the following steps:

1. Derive $V_{e_{0,0}}$, such as demonstrated in fig. 2.2.
2. Compute $p_{0,0}/p_{\text{inlet}}$, using the computed $V_{e_{0,0}}$.
3. Compute $p_{1,0}/p_{0,0}$, with $V_{e_{1,0}} = V_{v_{1,0}}$.
4. Combine the TF of elements to achieve the full desired TF: $p_{1,0}/p_{\text{inlet}} = p_{1,0}/p_{0,0} \cdot p_{0,0}/p_{\text{inlet}}$.

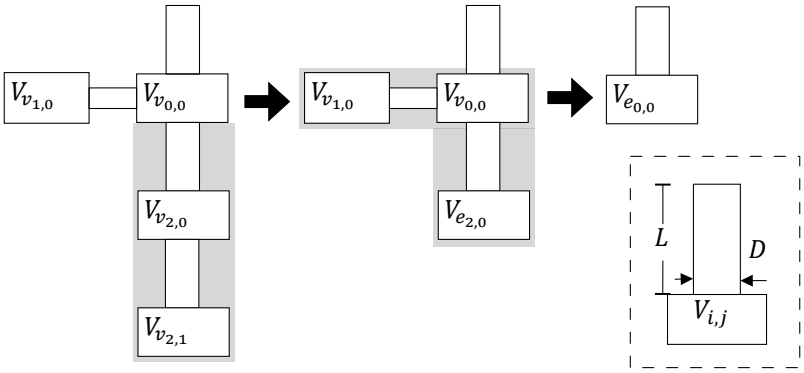

Figure 2.2: Illustration of the reduction of a parallel pneumatic-system geometry to its 'effective' impact on the upstream element (0, 0) with the W model. Tube-transducer elements have a coordinate (i, j), where i denotes parallel branches, and j denotes the serial element in the branch. Grey areas illustrate regions reduced to effective volume in the next step.

The limitations of the W model are linked to the linearization of the governing hydrodynamic equations and the assumptions used to simplify them, which are described in detail by Whitmore [10]. This means that the W model only provides accurate results as long as the assumptions are valid for the considered probe geometry and flow conditions.

Moreover, the W model, and most analytical one-dimensional models, assume high-aspect-ratio tubes, i.e., a length-to-diameter ratio greater than 10 [25], and laminar flow, i.e., small perturbations and internal flow velocities. Both assumptions are generally valid in the context of RMPs. Otherwise, Whitmore and Fox [23] offer a non-linear version of the W model. Gumley [25] provides eq. (2.2) as a pointer for the validity of the laminar assumption, where $\overline{U}_{tunnel}$ is the mean flow velocity in the outer flow region above the port:

$$L/\left(R^3\overline{U}_{tunnel}^2\right) > 1.6 \times 10^6\ \text{s}^2\ \text{m}^{-4}. \tag{2.2}$$

Furthermore, the process of longitudinal wave expansion within the tube is assumed to be polytropic. The gas properties and tube cross-section are assumed to be invariant over the section of the tube-transducer element. Still, these properties are allowed to vary from one tube-transducer element to another. Lastly, the cavity volume is considered to have a negligible length with respect to the tube length.

For fitting purposes, it is often recommended to non-dimensionalize the inputs of the system. If proper parameter combinations are chosen, these inputs will form an orthogonal system, where each input parameter has a unique and distinct effect on the system response compared to the other parameters. Say that the parameter combination L/R is often present in the model equations, then both L and R will affect the terms with which they are combined in an equal manner, albeit inversely. All sets of optimal parameter values will produce the same constant value for L/R. Therefore, to improve the convergence of the BI method, for the model of eq. (2.1), the input parameters are chosen to be: the (length) reduced frequency $k_{L,j}$, the shear wavenumber α_j, $(V_v/V_t)_j$, γ, Pr, c_i/c_j, and V_{t_i}/V_{v_j}. The first two parameters are inspired by Tijdeman [26], although the reduced frequency uses the tube length instead of its radius, which simplifies the model notation. The employed formulation is shown in eq. (2.3).

$$\begin{gathered} k_{L,j} = \frac{\omega L_j}{c_j} \qquad \alpha_j = i^{3/2} R_j \sqrt{\frac{\omega}{\nu_j}} \qquad \left(\frac{V_v}{V_t}\right)_j = \frac{V_{v_j}}{L_j \pi R_j^2} \\ \gamma_j = \left(\frac{c_p}{c_v}\right)_j \qquad Pr_j = \left(\frac{\nu}{\hat{\alpha}}\right)_j \qquad \frac{V_{t_i}}{V_{v_j}} = \frac{L_i \pi R_i^2}{V_{v_j}} \qquad \frac{c_i}{c_j} = \sqrt{\frac{\gamma_i \tilde{R}_i T_i}{\gamma_j \tilde{R}_j T_j}} \end{gathered} \tag{2.3}$$

Here, the kinematic viscosity is denoted ν. c_p and c_v are the heat capacity at constant pressure and volume, respectively. $\hat{\alpha}$ is the thermal diffusivity, $\tilde{R}$ is the specific gas constant, and T is the flow temperature.

Using the non-dimensional parameters defined in eq. (2.3), the W model can be rewritten in the fully non-dimensional form:

$$\begin{gathered} \left(\frac{V_e}{V_t}\right)_j = \left(\frac{V_v}{V_t}\right)_j \left[1 + \sum_{i=1}^{N} \Phi_{i,j}\right] \qquad \phi_j L_j = k_{L,j} \sqrt{\frac{J_0\langle \alpha_j \rangle}{J_2\langle \alpha_j \rangle}} \sqrt{\frac{\gamma}{n_j}} \\ \Phi_{i,j} = \frac{V_{t_i}}{V_{v_j}} \left(\frac{V_e}{V_t}\right)_i \left(\frac{c_j}{c_i}\right)^2 \frac{\cosh\langle \phi_i L_i \rangle + \sinh\langle \phi_i L_i \rangle / [\phi_i L_i (V_e/V_t)_i]}{\cosh\langle \phi_i L_i \rangle + \sinh\langle \phi_i L_i \rangle \cdot [\phi_i L_i (V_e/V_t)_i]}. \end{gathered} \tag{2.4}$$

For a pinhole probe, the effect of the three main geometrical parameters is shown in fig. 2.3. k_L is chosen here as the frequency axis. This parameter affects the line resonance of the pinhole, hence, its resemblance to other line resonance equations, such as for open-ended tubes in

$$f_{r,t} = \frac{c}{2L} \cdot n \quad \text{with } n \in \mathbb{N}_1 \quad \rightarrow \quad n\pi = \frac{2\pi f_{r,t} L}{c} = \frac{\omega L}{c} = k_L. \tag{2.5}$$

Both k_L and α contain the angular frequency. The former has resonance all along the frequency axis at its harmonics, hence its frequency dependence. The latter denotes the regime of the flow inside the tube, much like the Reynolds number in a Poiseuille flow. As noted by Tijdeman [26], the parameter α affects the flow profile inside the tube sections. Both k_L and α dictate the attenuation of pressure fluctuation inside the tubes. Naturally, α contains the kinematic viscosity, as such, this parameter can be used to change the overall viscosity of the model directly. Finally, V_v/V_t is the ratio of volumes in the cavity with respect to the volume in the tube. This parameter affects the cavity resonance of the tube-cavity system.

From fig. 2.3b, it can be seen that the smaller α_j, the larger the impact of viscosity. As mentioned by Tijdeman [26], the model for the propagation constant ϕ_j requires

$$\frac{R}{L} \cdot k_L \ll 1 \text{ and } \frac{R}{L} \cdot k_L / |\alpha| \ll 1.$$

From fig. 2.3b, it can be clearly seen that, for too large $|\alpha_j|$, the TF breaks down from a certain $k_{L,j}$ onward, $k_{L,j} = 6 \times 10^{-2}$ in this case. The effect of cavity resonance is clear in fig. 2.3c. Larger cavity-

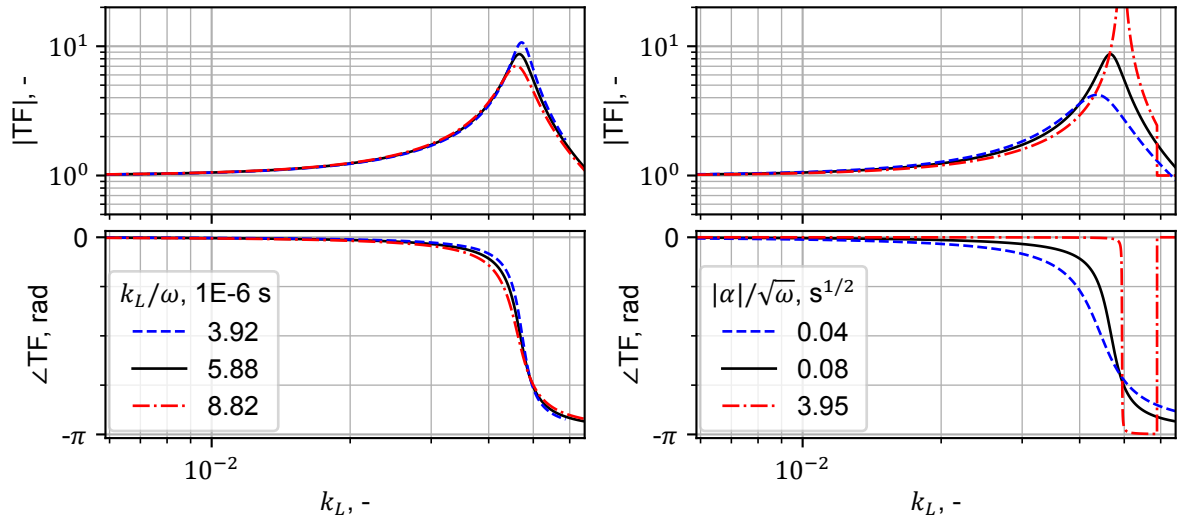

(a) Effect of k_L.

(b) Effect of α.

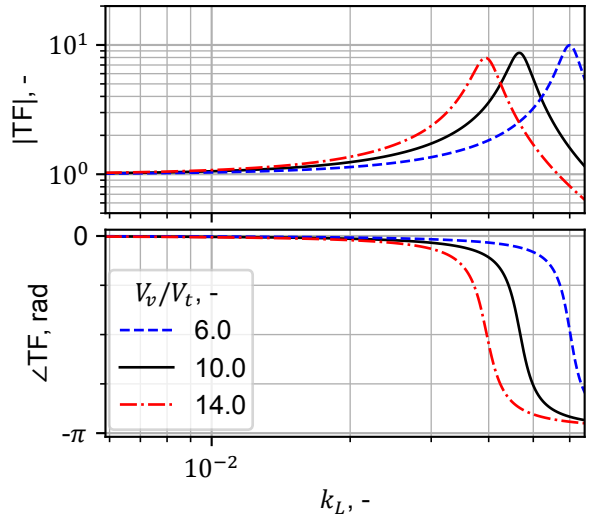

(c) Effect of V_v/V_t.

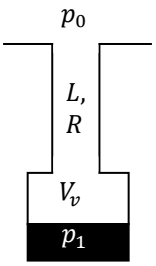

(d) Pinhole geometry. TF= p_1/p_0.

Figure 2.3: Effect of normalized parameters of the W model on a pinhole TF.

to-tube-volume ratios decrease the resonant frequency, as occurs for Helmholtz resonators in

$$f_c = \frac{c}{2\pi}\sqrt{\frac{A}{V_v L}} = \frac{c}{2L}\sqrt{\frac{V_t}{V_v}}. \tag{2.6}$$

Noteworthy is that the higher-frequency cavity resonance has a larger amplitude. Different k_L and α combinations result in different amounts of attenuation [26, p. 15]. The same effect is possibly part of the reason behind the solutions in fig. 2.3a not perfectly collapsing. Note that geometries with larger k_L will contain not only a possible cavity resonance but also tube resonance and its harmonics. This answers, in part, research question 2, on how a pinhole TF is affected by its geometry.

2.2. Bayesian inference

The second part of the analytic aspect of the semi-empirical calibration method is the BI method, which serves to couple the analytical model for the tube-transducer system to its empirical response. First, the reason behind choosing the Bayesian inference method over other simple 'curve fitting' approaches should be motivated. A functioning semi-empirical calibration method can be developed by simply iteratively changing the parameter values randomly and accepting these new parameter samples based on the quality of the model fit, e.g., quantified by the cumulative difference between the data and model.

Such a method uses a single information source: the empirical calibration data. Conversely, the BI method uses information from two primary sources: the empirical calibration data and the prior knowledge of the system. It aims to minimize the difference between the measurements and the model while also considering the probability of the parameter values needed for that fit.

An immediate benefit of the BI approach is achieved for systems with parameters that provide overlapping effects. With the W model, it has been shown that V_{v_j}/V_{t_j} has a direct impact on the TF of the probe. Consider only V_{v_j}/V_{t_j} for a model-fitting example, and assume that there is a true optimal value for V_{v_j}/V_{t_j}. Different combinations of the dimensional parameters (L_j, R_j, and V_{v_j}) would result in an equally good fit. A very short or very narrow tube would result in the same tube volume, hence the same V_{v_j}/V_{t_j}, impacting the TF in a similar way. No unique solution would emerge from the 'simple-fitting' method. The BI accounts for the probability of the parameter values and will prioritize combinations where each separate parameter is within a realistic range. As such, the fit of BI may be less close to the data than the 'simple-fitting' method, but the parameters, and thus the TF, are more likely to be physically correct. New, less probably, parameter values will be accepted only when the data show a large enough difference in fit quality.

The diagram in fig. 2.4 describes the concept behind the BI method. In both reality and analytical models, a RMP has several parameters: *geometric* (tube length, tube radius, cavity volume, tube-transducer topology, etc.) and *atmospheric* (mean density, Prandtl number, viscosity, heat-capacity ratio, speed of sound, grazing-flow velocity, etc.). The frequency response of the RMP system can be considered its state u and is defined when a set of parameter values $\overline{\alpha}$ is run through the model m, e.g., the W model. In this case, the system state can be thought of as a continuous function without any form of measurement error. By calibrating a pressure probe, one measures or samples this system state at specific frequencies. This sampling action of the state is defined by a sampling operator H, which will be explained later in the section. Measurements of the frequency response of a pressure probe can be seen as a summation of the true frequency response plus a measurement error ε. The exact amount of error is unknown and can take a range of values. Hence, the error is considered a probabilistic random variable (RV) with a probability density function (PDF). Following the process from left to right in fig. 2.4, a PDF describing the possible values of each measurement is obtained for a specific set of parameter values. When real measurement data are available, this PDF can be used to determine its probability of occurring, given the assumed parameter values.

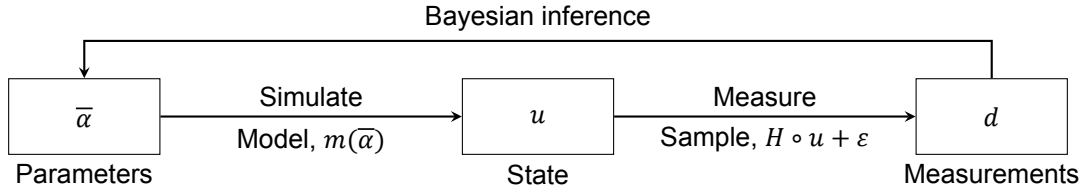

Figure 2.4: BI concept schematic.

If many experiments are performed, the PDFs of the measurement values can be computed without having to go through the process of fig. 2.4. This opens up the option to iterate the input parameter values through the model with the aim of getting PDFs of the measurements close to the observed ones. In essence, this is BI, which can be thought of as an inversion of the conventional process illustrated in fig. 2.4. The method infers the parameter values through the measurement data and a representative model of the system. Although various implementations of the procedure exist, all of them have the same PDFs at their base: the prior, the likelihood, and the posterior [27].

In eq. (2.7), Bayes' rule [28] is shown in the context of the measurement and parameter RVs used in BI. The model can have many parameters, hence, $\overline{\alpha}$ denotes the parameter vector. This also differentiates it from the notation of the shear wavenumber α. The model state u, measurements d, and measurement error ε are also vectors. The latter two with a dimension equal to the number of data points. The *model evidence* $\rho(d)$ can be further expanded using the law of total probability, i.e., $\rho(d) = \sum_{i=1}^{k} \rho(d|\alpha_i)\rho(\alpha_i)$, with k being the dimension of the parameter vector. All three aforementioned PDFs at the base of BI are present in this equation. Each of them is further explained in the following paragraphs.

$$\rho(\overline{\alpha}|D = d) = \frac{\rho(d|\overline{\alpha})\rho_0(\overline{\alpha})}{\rho(d)} \tag{2.7}$$

Each parameter value has a probability of occurring. $\rho_0(\overline{\alpha})$ is termed the prior PDF and is defined based on prior knowledge and assumptions. For example, repeated measurements of the length of the pinhole probe tube provide a normal distribution, which is characterized by a mean and variance.

Iterating over each parameter value gives the likelihood PDF $\rho(d|\overline{\alpha})$, which details the probability of observing specific measurements given the parameter value. Assuming that the error ε on each measurement d is independent and an identically-distributed Gaussian noise, the likelihood is simply a multivariate Gaussian PDF of the deviation of the measurements from the state, with a covariance operator R for the noise and a zero mean. The concept is expressed in mathematical form in eq. (2.8), and an example is presented in fig. 2.5a. The observation operator H is an interpolation matrix, which links the frequencies at which model and measurement data are available. For CFD simulations, the locations or spatial coordinates at which data are computed are dependent on the mesh and are different from the coordinates at which experimental data are available. In these cases, the operator H is a necessity. However, if the model can use the same locations as the measurements, the state needs to be sampled without interpolation, and H can be taken as a simple identity matrix.

$$d - H \circ m(\overline{\alpha}) = \varepsilon \sim \mathcal{N}(\overline{0}, \overline{\overline{R}}) \qquad \text{with } \overline{\overline{R}} = \sigma_d^2 \overline{\overline{I}}. \tag{2.8}$$

Lastly, the posterior $\rho(\overline{\alpha}|d)$ is the combination of both prior and likelihood, representing the probability of the parameters being those to have resulted in the observed measurements or the probability of the parameters given the measurements. This is the PDF that has to be sampled. Figure 2.5b provides an example of the prior and likelihood forming the posterior. The maximum a posteriori (MAP) estimate of the PDF, i.e., their absolute maxima, defines the most likely parameter values that result in the observed measurements. Equation (2.7) for the posterior is normalized with $\rho(d)$, which can be computationally expensive and only serves to scale the total probability of the posterior to one, $\int_{-\infty}^{\infty} \rho(\overline{\alpha}|d) d\overline{\alpha} = 1$. The various implementations of BI either use the local posterior slope or the ratio of the posterior for a new set of parameter values with respect to previous ones to steer the fitting algorithm to the MAP. For these BI methods, the posterior does not need to be normalized. Hence, the formulation that is actually used in BI is simplified to eq. (2.9). Strictly speaking, this means that also the prior does not need to integrate to unity to be usable in the context of BI, hence, the distribution can be artificially set to zero outside of the logical bounds of the parameters, e.g., for negative tube lengths.

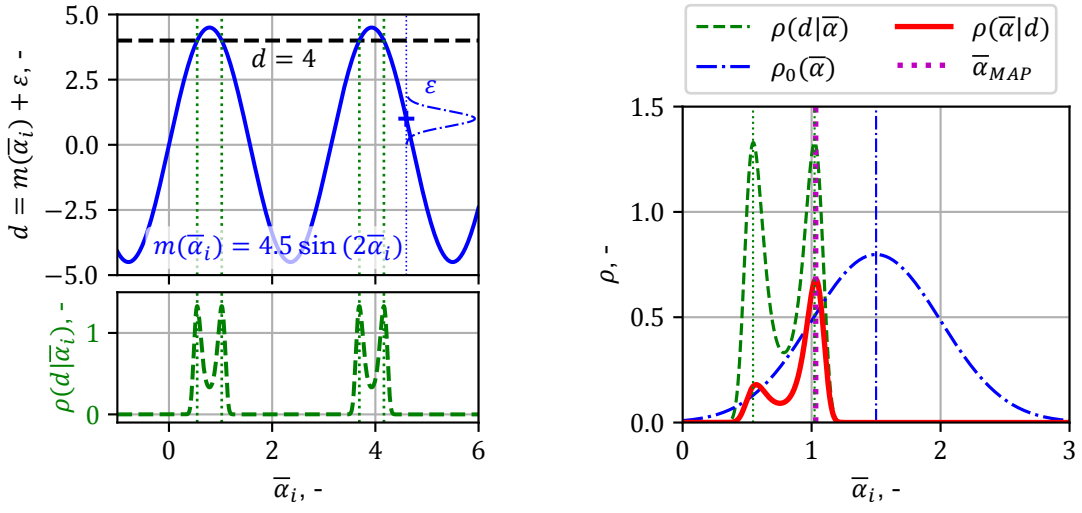

(a) Likelihood PDF.

(b) Posterior PDF.

Figure 2.5: BI example applied to a sine function measurement $d = 4$ with $\sigma_d = 0.3$ and $\rho_0(\overline{\alpha}_i) \sim \mathcal{N}(1.5, 0.5)$.

$$\rho(\overline{\alpha}|d) \sim \rho(d|\overline{\alpha}) \cdot \rho_0(\overline{\alpha}) \tag{2.9}$$

A closed-form formulation exists for the posterior when the model is linear and both prior and likelihood are Gaussian (see eq. (2.10)). For non-linear models, such as the W model, no simple equation exists for the posterior, and one needs to estimate the distribution by sampling the PDF. It is also impossible to assess all model solutions over the entire parameter space, as this is too computationally expensive, especially when using more advanced models. BI methods, therefore, estimate the posterior PDF by sampling around regions of high probability. Different implementations of BI offer different algorithms with which they explore the parameter space to find the MAP, each with its advantages and disadvantages. Two types of implementations are considered in this case: the gradient-ascent with adjoint method and the McMC method[1].

$$
\begin{gathered}
d = M\overline{\alpha} + \varepsilon \qquad \varepsilon \sim \mathcal{N}(\overline{0}, R) \qquad \rho_0(\overline{\alpha}) \sim \mathcal{N}(\mu, P) \\
\rho(\overline{\alpha}|d) \sim \exp\left[-\frac{1}{2}\left(d - M\overline{\alpha}\right)^T R^{-1}\left(d - M\overline{\alpha}\right)\right] \cdot \exp\left[-\frac{1}{2}(\overline{\alpha} - \mu)^T P^{-1}(\overline{\alpha} - \mu)\right] \sim \mathcal{N}(\hat{\mu}, \hat{\Sigma}) \\
\text{with } \hat{\mu} = \mu + K(d - M\mu) \quad \hat{\Sigma} = (I - KM)P \quad K = PM^T(R + MPM^T)^{-1}
\end{gathered}
\tag{2.10}
$$

The chosen implementation is the Metropolis-Hastings (MH) version of the McMC [29]. A major contributor to this choice is the ease of implementation since it works with random samples from the posterior instead of requiring any model-specific implementation. The MH algorithm, presented in algorithm 1, evolves towards regions of high probability by taking random steps based on the multi-variate Gaussian $\mathcal{G}$ centered on the current parameter value sample. Samples are accepted when the ratio of the posterior PDF at the newly proposed parameter sample over the value at the previous sample exceeds a random sample from the uniform distribution $y_i \sim \mathcal{U}(0, 1)$. As such, samples with a higher posterior PDF are accepted by default, ensuring that the chain keeps evolving in the direction of highest probability, which is demonstrated in fig. 2.6. Notable is that there exists a chance that the sample is accepted when the ratio is smaller than 1, resulting in some random sampling around the region of high probability, i.e., the sampling chain will not simply reside in the MAP of the posterior PDF.

Algorithm 1: Metropolis-Hastings, McMC.

Result: Markov chain, $\overline{\alpha}_i$ for i = 0, 1, ..., N
Initial guess parameters, $\overline{\alpha}_0$;
Initial posterior, $\rho(\overline{\alpha}_0|d)$;
for *i := 1, ..., N* **do**
  Sample parameters normally around previous sample, $\overline{\alpha}_p = \overline{\alpha}_{i-1} + \overline{g}_i$ with $\overline{g}_i \sim \mathcal{N}(0, \overline{\overline{P}})$;
  Posterior of sample, $\rho(\overline{\alpha}_p|d)$;
  Compute, $\Pi = \rho(\overline{\alpha}_p|d)/\rho(\overline{\alpha}_{i-1}|d)$;
  Sample uniform distribution, $y_i \sim \mathcal{U}(0, 1)$;
  if $y_i < \Pi$ **then**
    Accept sample, $\overline{\alpha}_i = \overline{\alpha}_p$;
  else
    Reject sample, $\overline{\alpha}_i = \overline{\alpha}_{i-1}$;
  end
end

This random sampling around the MAP is an additional benefit of McMC compared to gradient-ascent methods. The posterior PDF can be estimated from these samples using a kernel density estimate (KDE) method [30]. This allows the proposed calibration method also to give an estimate of the uncertainty of the TF fit with respect to the considered parameters. The uncertainty can then be propagated into the corrected pressure measurements and all the derived quantities. Compared to the standard calibration methods, this offers an additional major advantage. By contrast, the main disadvantage of McMC compared to a gradient-ascent with an adjoint method is that it scales badly with the number of fitting parameters. However, for the number of parameters considered for the proposed method, i.e., approximately less than 10, the scaling is not expected to pose too much of an issue.

[1]Dwight, R. P., "Uncertainty Quantification: Propagation and inversion in complex models," `https://aerodynamics.lr.tudelft.nl/~rdwight/cfdiv/index.html`, Apr. 2021. Accessed on: 27/08/2021.

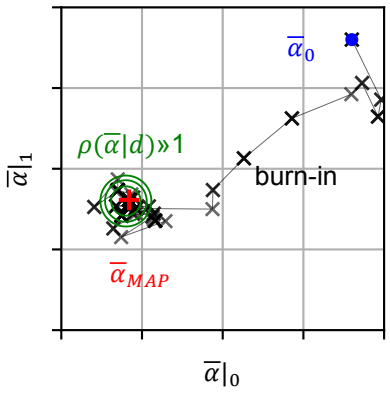

Figure 2.6: MH McMC sampling example with 100 samples, $\rho(\overline{\alpha}|d) \sim \mathcal{N}(\mu, \Sigma)$, $\mu = (0.2, 0.4)$, and $\Sigma = (0.05, 0.05)\bar{\bar{I}}$.

Two aspects of McMC are important to stress: the *burn-in* and the *sampling-operator step size*, the latter linked to the variance P of the sampling distribution Gaussian $\mathscr{G}$. As can be deduced from fig. 2.6, large step sizes will require fewer steps, i.e., fewer model evaluations, to reach a region of a high probability of the posterior PDF from a given initial guess. Naturally, the further the initial guess is from the MAP, the more steps are required to reach it. The steps needed to reach the region surrounding the MAP are termed burn-in. These samples do not reflect the posterior PDF and are thrown away before computing the KDE. Once the region of high probability is reached, the region is sampled to reconstruct the posterior PDF. The acceptance rate of samples will decrease along with the step size as the samples are more likely to land in regions of low probability. Inversely, a small step size increases the acceptance rate. However, the step size also influences the correlation between the samples. If the KDE of the samples is used to estimate the posterior PDF, the sample distribution in the parameter space needs to reflect the posterior and not the sampling Gaussian. Hence, if an accurate estimate of the uncertainty of the fit with respect to the parameters is desired, then the chain might need to be resampled. Once the high-probability region is reached, many uncorrelated samples have to be taken in this region in order for the KDE to provide an accurate estimation of the PDF. This is because the KDE is a Monte Carlo estimator, much like eq. (2.11) is a Monte Carlo estimator for the expectation of the random variable X of which x_i are random samples. Such Monte Carlo estimators use random samples to estimate statistical quantities, and therefore need N samples to converge to a fixed value, or PDF estimate in the case of the KDE. The number of required samples differs from case to case.

$$E[X = x_i] = \frac{1}{N}\sum_{i=1}^{N} x_i \tag{2.11}$$

2.3. Implementation of BI to W model

As mentioned in section 2.2, the parameters $\overline{\alpha}$ can encompass any desired parameters from the analytical model, e.g., geometric or atmospheric. The model or system state u defined by a set of parameter values can be thought of as the frequency response function of the probe. The state is not the TF at discrete frequencies but the continuous function that defines the true frequency response without measurement error, such as the calibrator-induced spurious resonance.

The measurement d is then the result of sampling the system state u at discrete frequencies plus the error ε made in the calibration process. This measurement vector is complex-valued, and it is simpler to consider these two signals as two measurement vectors, i.e., the amplitude and phase. Moreover, the measurement error variance σ_d in both vectors is interlinked. However, allowing both error variances to be set independently enables the operator to prioritize the fit with either one of these two measurement vectors.

The prior PDF is another tool that can be used to improve the model fit to the data. Any type of PDF can be chosen, and the PDF does not even need to integrate to unity, as mentioned in section 2.2. The least informative PDF to the fitting process is simply a uniform distribution, which sets extremes to the possible range of parameter values. Slightly more informative to the BI process is a normal distribution,

which requires a mean and variance to be defined by the user. Both uniform and normal distributions can be multiplied as well, or even more complex PDFs can be defined.

2.4. Goody model

For pinhole probes, the TF from the calibration data and the semi-empirical method can be compared to the known theoretical TF. However, for more complex RMPs, a second point of comparison is needed to evaluate whether the removed frequency bands are actually spurious and whether the new TF provided by the model physics is correct. The expected WPS of a zero-pressure-gradient (ZPG) flat plate turbulent boundary layer (TBL) is well-documented. Hence, the unsteady wall-pressure fluctuation measurements acquired with the RMP can serve as a benchmark, allowing the two TFs to be compared to a theoretical reference WPS. A quantitative error that is not affected by the TF of the probe can be defined between the calibrated WPS and the theoretical WPS. Defining the error of the calibration approach in this manner is quite natural, as the goal of the calibration is to remove the impact of the probe TF on the pressure measurements. Any error that remains in the TF propagates to the WPS.

This theoretical reference ZPG TBL WPS can be found in models that provide the WPS for the given flow parameters. The model that will be used for the current investigation is that of Goody [19]. It is an empirical model based on data from several research groups, spanning a Reynolds number range of $Re_\theta \in (1.4 \times 10^3,\ 2.34 \times 10^4)$. The change in the range of relevant scales with Reynolds number is accounted for using the ratio of timescales parameter R_T. The model is shown in eq. (2.12). The dimensional WPS is Φ, U_e is the velocity at the edge of the boundary layer, τ_w is the wall shear stress, δ^* is the displacement thickness, R_T is the ratio of timescales of the unsteady pressure, δ is the boundary layer thickness, u_τ is the friction velocity, and C_i are model constants.

$$\frac{\Phi(\omega)U_e}{\tau_w^2\delta^*} = \frac{C_2\left(\omega\delta^*/U_e\right)^2}{\left[\left(\omega\delta^*/U_e\right)^{0.75} + C_1\right]^{3.7} + \left[C_3\left(\omega\delta^*/U_e\right)\right]^7} \tag{2.12}$$

$$C_1 = 0.5 \qquad C_2 = 3.0 \qquad C_3 = 1.1R_T^{-0.57} \qquad R_T = \frac{\delta/U_e}{\nu/u_\tau^2}$$

As proposed by [14], the model is reformulated using the displacement thickness instead of the boundary layer thickness, following the relation $\delta^* = \delta/8$ from the 1/7$^{\text{th}}$ power-law canonical mean velocity profile. This alteration is proposed due to the improved robustness when computing the displacement thickness from experimental data compared to the boundary layer thickness.

In comparison with a WPS model, the WPS measurements are corrected for averaging of the measured unsteady pressure fluctuations due to the finite size sensing area, following the model of Corcos [8]. The convection velocity U_c for this model is estimated using the model of Smol'Yakov [31]. The remaining model parameters are derived from the hot-wire anemometry (HWA) measurements, which are further discussed in section 3.5.

3

Methodology

Calibration data are required to test the proposed method, learn about its strength and limitations, and answer the research questions aimed at understanding the workings of the method. Several datasets used to analyze the proposed method in chapter 4 originate from previous unpublished experimental campaigns at the von Karman Institute of Fluid Dynamics (VKI). Two new datasets are presented, a FEM simulation, detailed in section 3.1, and a measurement campaign with a RMP. The RMP-dataset experimental setup contains four elements: (i) the plane-wave tube calibration method in section 3.2, (ii) a wind tunnel detailed in section 3.3, (iii) the RMPs used to acquire unsteady wall-pressure measurements in the wind tunnel in section 3.4, and (iv) the hot-wire anemometer setup used to acquire the boundary layer over the wall in section 3.5.

3.1. FEM simulation

For the FEM dataset presented in section 4.1, an acoustic FEM simulation of the plane-wave tube calibrator is performed. The exact geometry is shown in fig. 3.1. The calibrator is further discussed in section 3.2. The acoustic and vibroacoustic solver used is the NASTRAN SOL 108 (Direct Frequency Response) equation set, implemented in Siemens Simcenter.

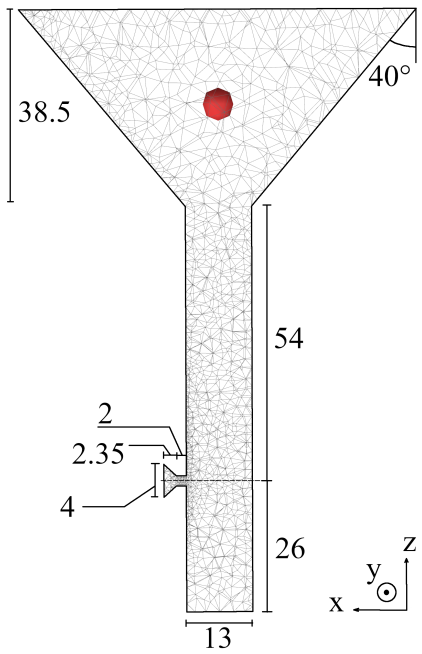

Figure 3.1: Cross-section of the FEM geometry, consisting of cylinders and cones. The red dot in the speaker cone represents the acoustic monopole. The dimensions are provided in mm and degrees.

The physics of the speaker is simplified for this dataset. The solver can model the speaker membrane as a vibrating surface, hence, generating pressure waves in this manner. For this to occur, the membrane must reflect pressure waves. However, to accurately define its reflective characteristics, the impedance of the surface must be known. Instead, the speaker membrane surface does not vibrate and is made into an anechoic boundary, i.e., an **automatic matched layer**. The pressure waves are generated by a monopole situated midway in the plane-wave tube calibrator speaker cavity, represented by the red dot in fig. 3.1. All other boundaries are set to perfectly reflect pressure waves.

The geometry is discretized with $25\,422$ tetrahedral elements, ranging from 0.7 mm to 3.5 mm in size. The smallest elements are situated in the side-branch pinhole, and the largest ones are in the speaker cavity. By considering the rule-of-thumb according to which approximately 6 to 10 elements per wavelength are required, accurate results should be achievable up to 16.2 kHz to 9.7 kHz.

3.2. Plane-wave tube calibration method

An empirical calibration method is needed for the base of the method. For the empirical calibration, the same set-up as used by Van de Wyer et al. [14] is employed and is shown in fig. 3.1. The steel plane-wave tube has a main channel over which a speaker (Monacor model SPH-75/8) sits connected by a large conical cavity. A small pinhole side branch in the main channel connects to a cavity containing the calibrator microphone. The open end at the bottom of the main channel is placed over either the RMP or flush-mounted reference microphone.

The datasets in section 4.2 and section 4.3 originate from previous experimental campaigns at VKI, which employed the same steel calibrator. These datasets, along with the data in fig. 4.13, use Brüel & Kjær type 4938 microphones connected to a Brüel & Kjær Nexus. Instead, the electret pinhole probe uses a Knowles FG-23329-C05 coupled to a custom VKI-built amplifier. For the RMP data in section 4.5, the original plane-wave tube is modified to have an additional side branch located 13.5 mm from the open bottom end of the main channel. This lower side branch of the calibrator has the same dimensions as the upper side branch, albeit with a smaller pinhole radius of 0.35 mm. For these measurements, except for the aforementioned fig. 4.13, all calibrator and reference microphones are quarter-inch GRAS 40PH microphones.

The speaker signal is generated by an Agilent 33120A and amplified with a JBL UREI 6230. In section 4.2 and section 4.3, a repeating logarithmic frequency sweep is acquired for a total of 30 s, spanning from 0.1 kHz to 15 kHz in 2 s and 1 s, respectively. In section 4.5 a white-noise signal is acquired for a total of 70 s.

For all cases, the signals are acquired at 51.2 kHz using a LabVIEW VI, with a National Instruments 9234 acquisition card in a National Instruments cDAQ-9174 acquisition board. The sensitivity of all microphones is estimated using a Brüel & Kjær pistonphone Type 4231, which emits a predefined sinusoidal signal with a frequency of 1 kHz and an amplitude of 1 Pa, i.e., ≈ 94 dB using a reference pressure of 20 µPa. Transfer functions are computed using the method of eq. (1.2), i.e., a Python implementation of the MATLAB 'tfestimate' function.

3.3. Wind tunnel: WAABLIEF

The wall-pressure spectrum (WPS) is acquired to analyze the impact of calibration-induced spurious resonance on measurements corrected with these affected calibrations. In addition, the measured WPS and velocity profiles over solid and porous wall inserts constitute a dataset for the validation and calibration of a numerical simulation of flow over and through porous materials. The WAABLIEF wind-tunnel (**W**ind tunnel for **A**ero**A**coustic **B**oundary **L**ayer **I**ncluding pr**E**ssure gradient e**F**fect) [14], shown in fig. 3.2, offers a controlled measuring environment with low noise, which is ideal for highly-accurate pressure measurements. The maximum achievable velocity is around $30\,\mathrm{m\,s^{-1}}$.

Furthermore, a trip consisting of three 1 mm strips of sandpaper with 1 mm gaps between them is placed near the inlet of the test section, 0.15 m upstream of station 0. This trip is used to force the laminar-to-turbulent flow transition of the boundary layer, making the transition point independent of the conditions and achieving a more consistent inflow in the test section. This also facilitates the comparison between numerical simulations of the wind tunnel flow and the measurements, as the transition point is known and determined by the trip location.

The center of the measurements coordinate system is located at the center of station 2, on the lower wall in fig. 3.2, ca. 1.4 m downstream of the boundary-layer trip. Near the inlet of the test section, in

station 0, a thermocouple and a static pressure port are installed. A total pressure port is located near the meshes (see fig. 3.2) at the inlet of the tunnel. Both static- and total-pressure ports are used to acquire the inflow velocity at the inlet. More information on the facility can be found in Van de Wyer et al. [14], which employs a previous version of the wind-tunnel inlet.

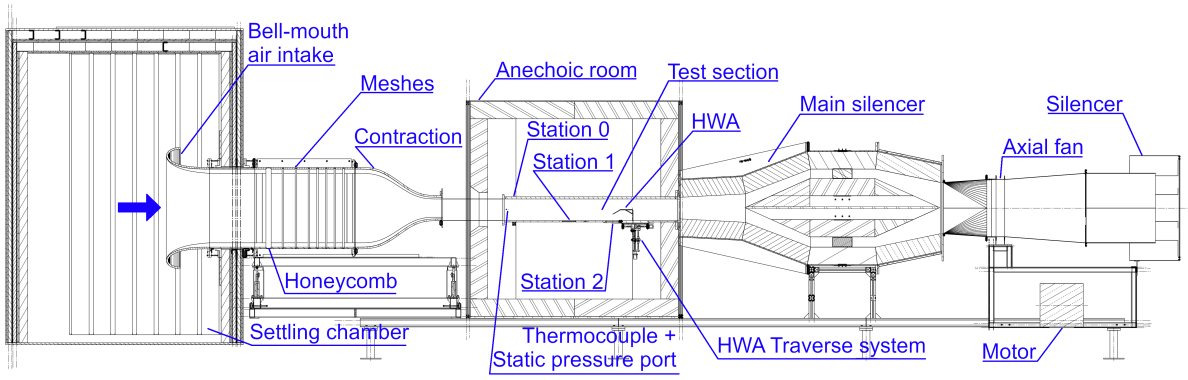

Figure 3.2: WAABLIEF wind tunnel schematic. The stations in the test section allow for the mounting of the measuring equipment and testing geometry.

3.4. RMP: Semi-infinite waveguide probe

The WPS measurements on a solid plate are acquired as part of a larger experimental campaign, which includes boundary-layer measurements over porous wall liners. Three microphone probes sit flush with the upper surface of the solid or porous liner, located at -33.3 mm, 0 mm and 33.3 mm, while two probes sit flush with the lower liner-cavity surface and are located at -16.7 mm and 16.7 mm. This is shown in fig. 3.3a. Naturally, for the solid plate, only the signals from the three upper surface microphones are meaningful.

The RMPs are semi-infinite waveguide probes. As shown in fig. 3.3b, the inlet orifice of the probe is connected to a very long capillary tube with a close to anechoic termination, by virtue of its ca. 2 m to 4 m length. At a certain distance along the main capillary tube from the probe inlet, a side branch is installed with a GRAS 40PH microphone, which exhibits a flat frequency response from 10×10^{-3} kHz to 20 kHz, within ± 2 dB. The main channel is constructed from a metallic tube from the orifice of the probe until 20 mm from the RMP side branch. A plastic capillary tube is slipped over the end of the metallic tube, which might lead to a small discontinuity in tube radius, hence reflections.

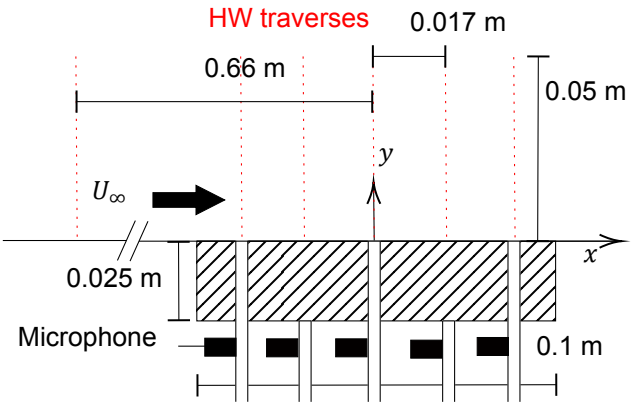

(a) RMP and HWA traverse locations in station 2, see fig. 3.2. Solid or porous wall insets are shown with dashed rectangles. The global coordinate system is indicated as well.
Dimensions in m.

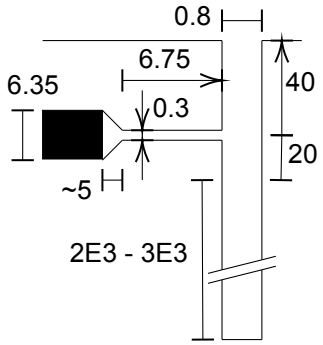

(b) RMP geometry in mm. Attenuation tubes vary in the region of 2 m to 3 m, and the depth dimension of the transducer cavity is a very rough estimate. A plastic capillary tube is slip-fit over a metallic one 60 mm from the RMP orifice.

Figure 3.3: Diagrams of the RMP location and dimensions of the HWA traverse coordinates. Diagrams not to scale.

3.5. HWA setup

The Goody [19] model is to be used as a theory-based comparison to the acquired and calibrated WPS. The model requires several BL parameters. Therefore, a single-component constant-temperature HWA is used to acquire the BL profiles over the microphone probes, as prior attempts with PIV did not return accurate velocity measurements very close to the wall. As shown in fig. 3.3a, five vertical profiles centered around the liner are acquired ($x/L = \{-0.33,\ -0.17,\ 0,\ 0.17$ and $0.33\}$, $L = 10$ cm), with a single profile to characterize the inflow conditions ($x/L = -6.6$), all at the center-span of the test section ($z/L = 0$).

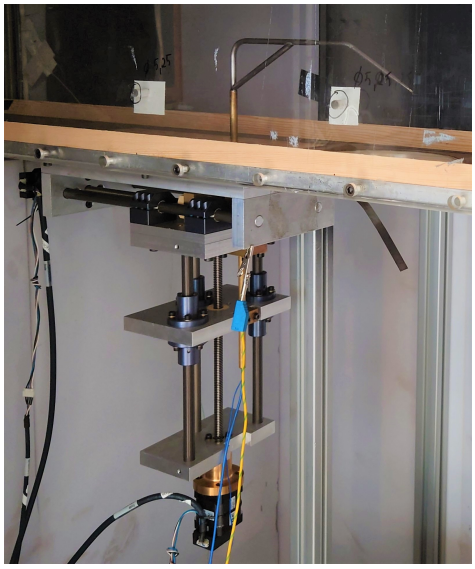

(a) HWA probe and robotized traverse used for the measurements, except the upstream traverse ($x/L = -6.6$).

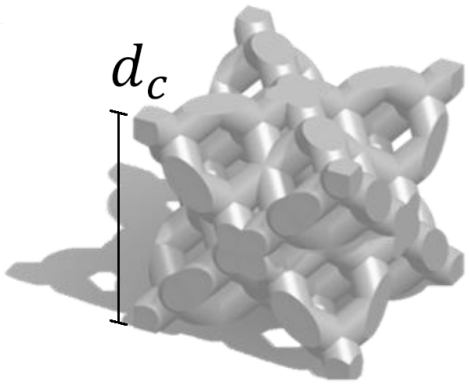

(b) Porous DMND liner unit, with cell sizes of $d_c = \{3.5\,\text{mm}, 4.5\,\text{mm}\}$.

Figure 3.4: HWA traverse system and porous liner CAD figure.

The two porous liners that are tested have a SLA 3D-printed DMND structure with a $62\,\%$ porosity. The structure of these liners has been specifically designed for the EU-funded project INVENTOR, which aims to research innovative flow-permeable materials for the reduction of aerodynamic noise radiated by high-lift devices. The porous structure is scaled to the cell size d_c, shown in fig. 3.4b, which is either 3.5 mm or 4.5 mm. The higher bound of permeability of the liner is around $1 \times 10^{-8}\,\text{m}^2$.

A different traverse system is used for the main five profiles and the upstream profile since the downstream traverse system is made for station 2 and, therefore, does not fit in station 1. For both setups, the probe uses a 9 µm tungsten wire with an overheat ratio of 0.8 and the DANTEC StreamLine Pro system for signal preprocessing and Wheatstone bridge. The dynamic and static calibration of the sensors are also performed through the DANTEC StreamWare Pro with a StreamLine Pro Automatic Calibrator. Both probes achieve a maximum sampling frequency of ca. 10.6 kHz at the maximum velocity of $28\,\text{m}\,\text{s}^{-1}$.

The measured voltage is corrected for thermal effects using the correction of Kanevče and Oka [32]. The method uses eq. (3.1) to estimate the voltage $E_{w,\text{ref}}$ that would be measured at a reference temperature $T_{a,\text{ref}}$, considering the wire temperature T_w, the flow temperature T_a, and the measured voltage E_w:

$$E_{w,\text{ref}} = E_w \left[\frac{T_w - T_{a,\text{ref}}}{T_w - T_a} \right]^{1/2}. \tag{3.1}$$

The wire temperature is estimated following eq. (3.2) from Zamponi [33]. This method uses two sets of HWA voltages and thermocouple temperature measurements performed at the same flow velocity:

$$T_w = \frac{E_{w,1}^2 T_{a,2} - E_{w,2}^2 T_{a,1}}{E_{w,1}^2 - E_{w,2}^2}. \tag{3.2}$$

The probe used for the five liner-centered vertical profiles has a third prong that sticks out 0.1 mm below the wire and closes an electrical circuit when it contacts a conductive surface to which the other side of the circuit is grounded. This probe also uses a 2D (XY) robotized traverse system with a spatial resolution of 5×10^{-3} mm, resulting in an accuracy of the y-coordinate of $\pm 2.5 \times 10^{-3}$ mm. Aluminum tape with a thickness of 1.3×10^{-1} mm is used for the height calibration on the porous liners. Each streamwise vertical profile has its height calibrated separately.

The upstream profile uses a probe without such a 'height calibration' prong and a manual traverse system. A counter attached to the traverse system crank serves as a visual indicator of the vertical coordinate. The counter is zeroed at the wall by sliding a piece of 1×10^{-1} mm paper under the probe wire. It is estimated that the visual indicator has an uncertainty of a quarter of a number on the counter, as the middle position between two numbers on the counter can still somewhat be easily read. Therefore, the estimated uncertainty on the y-coordinate of the upstream HWA measurements is ca. $\pm 6 \times 10^{-2}$ mm.

The vertical profiles are sampled with a logarithmic spacing of the y-coordinates close to the wall and a linear spacing towards the end of the logarithmic region of the BL, where the wake component starts to appear. As such, the switch to linear point spacing is at $y^+ > 7.1 \times 10^2$ for the five liner-centered profiles and at $y^+ > 3.7 \times 10^2$ for the upstream profile, both at $U_e = 25\,\mathrm{m\,s^{-1}}$. The minimum height for the five liner-centered profiles is 1.5×10^{-1} mm, or ca. $y^+ = 8.8$, for the solid-wall case at $U_e = 25\,\mathrm{m\,s^{-1}}$. The upstream profile has a minimum height of 4.7×10^{-1} mm, or ca. $y^+ = 23$ at $U_e = 19.2\,\mathrm{m\,s^{-1}}$, i.e., the upstream outer-flow velocity equivalent to an outer-flow velocity of $25\,\mathrm{m\,s^{-1}}$ over the liner at $x/L = 0$. Both the five liner-centered and upstream profiles acquire their vertical profiles starting from the maximum y-coordinate of 50 mm and descending towards the wall. After acquiring the point closest to the wall, the starting point of the profile is acquired again as a duplicate point for thermal corrections of the acquired HWA voltage signal. For all the solid-wall measurement cases, the height calibration of the profiles is further tweaked a-posteriori by comparison of the inner-scaled BL profile with the theory of ZPG TBL profiles.

During the measurements, for each probe point, the HWA voltage is sampled at 25.6 kHz for 10 s using the aforementioned NI cDAQ-9174 with NI 9234 cards for the HWA, and an NI 9211 card for the E-type thermocouple. The latter is sampled at 1 kHz over the same duration. The acquisition is performed through a LabVIEW VI, which acquires all the data channels and controls the robotized traverse system. A 2 s delay is imposed between the movement of the HWA probe to the desired coordinate and the acquisition at this coordinate.

Lastly, the statistical uncertainty of the mean velocity at each probe point is estimated using eq. (3.3), and the uncertainty on the turbulent intensity (TI) is calculated using eq. (3.4). This method is employed by Zamponi [33], and derived from Bendat and Piersol [34]:

$$\overline{U} \in \left(\overline{U} - \varepsilon_{\mathrm{CL}} \frac{\sigma_U}{\sqrt{N}},\ \overline{U} + \varepsilon_{\mathrm{CL}} \frac{\sigma_U}{\sqrt{N}} \right); \tag{3.3}$$

$$TI \in \left(\frac{100}{U_e} \sqrt{\frac{(N-1)\sigma_U^2}{\xi^2_{N-1,\,\alpha_{\mathrm{CL}}/2}}},\ \frac{100}{U_e} \sqrt{\frac{(N-1)\sigma_U^2}{\xi^2_{N-1,\,1-\alpha_{\mathrm{CL}}/2}}} \right). \tag{3.4}$$

HWA measurements in station 2 at $U_e = 20\,\mathrm{m\,s^{-1}}$ are shown in chapter 5.

3.6. Semi-empirical method code

The McMC method used in chapter 4 is the parallel **Para**llel **D**elayed-**R**ejection **A**daptive **M**etropolis-Hastings (ParaDRAM) McMC method of Haario et al. [35], which is fully implemented in Python by Shahmoradi et al. [36]. This parallelized sampler provides better computational performance than the serial equivalent. The same concepts regarding sampler step size and acceptance rate, explained in section 2.2, apply to ParaDRAM. A new posterior PDF is defined for each dataset, using a code based on the W model from eq. (2.1) and eq. (2.4).

The prior mean is defined as equal to the initial guess of the McMC. The initial guess is defined based on CAD files, e.g., fig. 3.1, or simple measurements of the physical probe dimensions. For some datasets, the initial guess is set to the MAP parameters of a previous McMC run, as this resulted in a better convergence. For simplicity, all atmospheric parameters are set to International Standard Atmosphere conditions.

For the sake of repeatability, the random seed is set to 3751 for all results presented. The target acceptance rate of the adaptive sampler is set to $10\,\%$ to $31\,\%$, with an adaptive update period of 50 iterations. The $30\,\%$ maximum is a rule of thumb, balancing the number of accepted samples and the correlation between samples. A lower acceptance rate can provide better computational performance for parallel sampling methods.

4

Results

In theory, if the model physics fully encompasses those that affect the frequency response of the probe, in reality, a perfect fit of the model with the calibration data exists. This fit contains all resonance linked to the probe itself and omits any resonance that cannot be produced by the considered probe under small changes in its parameters. The implementation of the method and the chosen model dictate whether or not the method can achieve said goal. Therefore, several datasets are presented with the aim of answering this question. Each dataset presents the strengths and limitations of the method differently as well.

First, in section 4.1, the method is benchmarked in the context of optimal artificial conditions created by an inviscid FEM simulation of a pinhole probe and RMP. The contrast of the inviscid simulation with the 1-D analytic model presents the possibility to comment on the validity of the model assumptions in the context of the TF of a probe. Second, real calibration data are analyzed, each with different spurious resonance and different challenges to the method. The considered datasets range from the simplest pinhole probe with a microphone with a 'flat' TF in section 4.2, to a pinhole probe with a microphone with a distinctly non-'flat' TF in section 4.3, to a branching RMP in section 4.5.

4.1. FEM dataset

From a single FEM simulation, two probe TFs are extracted. The pinhole probe is made from the side branch of the RMP. Both TFs are presented in fig. 4.1.

The TF provided by the model fit in fig. 4.1 adequately represents the data: (i) the resonant frequencies are matched, and (ii) the amplitude and phase are the same except at the resonant frequencies. In short, the model physics seems to sufficiently represent the mechanisms affecting the TF of the simulated probe. Still, only the real-life datasets can confirm if the method models the physical phenomena present in the calibration data.

Additionally, the match between the model and data indicates that the theoretical assumptions are valid. Although the simulation data and W model present the inverse assumptions, the latter being viscid but 1-D, all the resonant frequencies present in the data are matched by the model, indicating that no transversal resonant modes are present in the pinhole or RMP tubes. As such, the 1-D assumption is verified. For this to be the case, several model assumptions need to be valid [9]: (i) the tube radius needs to be small with respect to its length, and (ii) the flow inside of the probe needs to be laminar. As noted by Gumley [25], these same limitations are required to contain the end effects on the TF of the tube-transducer sections. In contrast, the effect of viscosity through the shear wavenumber α is much more pronounced, especially around the resonant frequencies.

An decrease in $|\alpha|$, i.e., $R\nu^{-1/2}$, reduces the resonant amplitude and resonant phase-shift slope. The likelihood PDF seeks to minimize the discrepancy between the model and the data, $d - H \circ u$. If the dimensional W model were used without ν as a parameter, then the radius would increase in perpetuity to emulate an inviscid response, whereas the cavity volume would increase with the radius to keep the same resonant frequency. For the non-dimensional W model, ν is included within the parameter α. Therefore, only $|\alpha|$ indefinitely keeps increasing in value to emulate an inviscid response. The indefinite stepping of the Markov chain implies that it will never converge to a MAP, hence, the KDE will

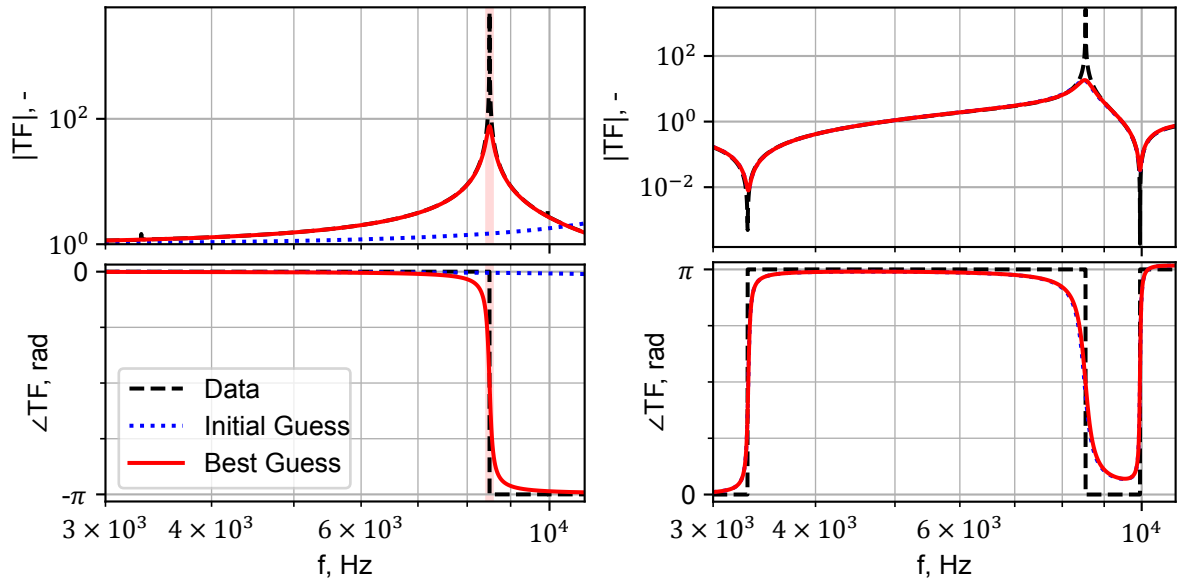

(a) Pinhole. $TF_{junction \to cal.}$.

(b) RMP. $TF_{flush \to cal.}$.

Figure 4.1: TF from FEM simulations of the plane-wave tube geometry, used as fitting data for the W model. 'Junction' is the point in the main channel of the calibrator, at which the side branch of the calibrator connects. 'Flush' is the point at the center of the lower boundary of the main channel of the calibrator. 'Cal.' is the point at the center of the boundary at the end of the calibrator side branch. The red-tinted region from 8.4 kHz to 8.6 kHz is band-removed for the pinhole case.

also never converge to a representative approximation of the posterior PDF, as the 'burn-in' samples are not representative of the posterior. The convergence of the chain can be ensured by band-removing the region around resonant frequencies (see fig. 4.1a) and/or strengthening the impact of the prior on the posterior by decreasing the variance of the prior and/or increasing that of the likelihood.

From one perspective, the FEM case presents the most difficult dataset to fit. With reference to research question 3, the TF fit is strongly affected by the implicit assumption that the TF data are influenced by viscosity, which is untrue for this dataset. Inviscid resonance is not physical and can be thought of as physically correct viscid resonance superimposed by spurious resonance. The aim of the method is to find the physically-correct TF while not including the spurious resonance in the fit. The problem here is that there is no clear delimitation between the spurious element and correct resonance, as the model can represent a range of α, and the spurious and correct resonance fall on the same frequencies. Therefore, for the method to converge on the considered data, more operator intervention is required than with real calibration data having calibrator-induced spurious resonance. This operator intervention comes in the form of adapting the BI settings or preprocessing (see research question 4) the data presented to the BI, e.g., band-removing spurious resonance.

Table 4.1: Difference between the McMC parameter MAP values and the FEM geometry.

Parameter	$(L/c)_{\text{lower}}$, s	$(V_v/V_t)_{\text{side}}$, -
MAP	7.52E-5	9.39 (RMP), 9.68 (pinhole)
FEM	7.64E-5	2.74

As mentioned above, the pinhole probe is a sub-element from the RMP in the FEM geometry, i.e., the dimensions of the RMP side branch and pinhole are identical. Notably, the different $(V_v/V_t)_{\text{side}}$ of the MAP for both cases in fig. 4.2 still differ from the actual value of the FEM geometry. Bergh and Tijdeman [9] mention that the tube radius of the model geometry with a matching TF to the calibration data tends to be 2 % to 5 % smaller than their real-life counterparts. The vast difference presented in table 4.1 requires another explanation. One possible source of the discrepancy could be the covariance between α and both geometrical parameters k_L and (V_v/V_t). Some coupling between how the parameters affect the TF of the probe still remains, even after the normalization of the model. In fig. 4.2a, the covariance of the posterior indicates that larger α require larger values for (V_v/V_t) to retain the same resonant frequency. The RMP case has a lower value for $|\alpha|$ than the pinhole case, 0.262 with respect to 0.679,

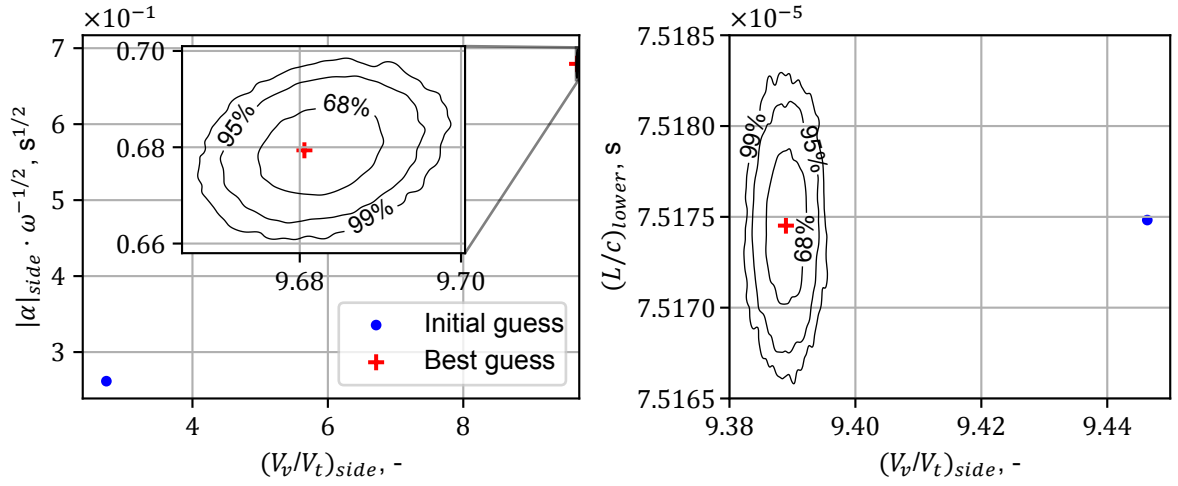

(a) Pinhole.

(b) RMP.

Figure 4.2: KDE of posterior samples from McMC of two FEM datasets, see fig. 4.1.

and a lower value for (V_v/V_t). Comparatively, the concept of $|\alpha|$ is problematic for the inviscid FEM data, but there is no guarantee that this is the only reason behind the discrepancy in MAP values.

A positive aspect of the KDEs in fig. 4.2 is that they appear to converge to a narrow uni-modal PDF, i.e., the high-probability region is defined by a narrow peak with a single maximum. This means that the method is well informed by the data, i.e., only a limited range of parameter values leads to a good fit.

All the calibration data presented in the following sections of this chapter use the two-step calibration approach discussed in section 3.2. The TF in fig. 4.1b is actually one of the two steps of said calibration approach and can, therefore, be used to investigate research question 1. The spurious resonant frequency found in the later datasets, e.g., fig. 4.6, well agrees with the 3.3 kHz and 10 kHz line resonance found in fig. 4.1b, which corresponds to the calibrator tube-section between its bottom port and the side branch. Minimizing this distance will push the spurious resonant modes to higher frequencies, but even 8.5 mm will push the resonant first mode to 10 kHz. This is not always feasible, as the calibrator should still fit the large-diameter flush-mounted microphones and produce plane waves over the relevant frequency range. Clearly, it is often not possible to solve this issue by solely acting on the calibrator design.

As described in research question 10, a different calibrator concept could be used not to run into the issues described in chapter 1 that induce spurious resonance. Basten and de Bree [37] place both the probe being calibrated and the reference microphone at an equal distance and direction from a sound source without any enclosure, such as the plane-wave tube. However, compared to the plane-wave tube calibrator, this open-air calibration method appears a lot more involved. It requires a combination of low-frequency and high-frequency calibration. Any external noise is also more likely to affect the calibration, as there is no plane-wave tube to create a controlled environment. Slight errors in the alignment of both the reference microphone and the probe-to-calibrate to the sound source also introduce errors in the calibration, thus a lot more effort is required in setting up the calibration process. Hence, it is believed that the semi-empirical calibration method, in combination with plane-wave calibrator data, can provide accurate results in a consistent manner.

Figure 4.1b also plays into research question 12. It indicates that the upper section of the calibrator, above its side branch, appears to have no influence on the response of the lower sections. Whatever pressure waves travel through the main channel of the calibrator up to the speaker cone and reflect back to the junction with the side branch are sent to both the side-branch microphone and the lower flush-mounted reference microphone. As such, these additional reflections caused by the closed-off upper geometry of the calibrator are added to the speaker signal as an additional pressure disturbance sent to both microphones. It could be said that the upper boundary of the calibrator is modeled as anechoic, thus open. However, the conclusion does not change. The line resonance linked to the main channel of the calibrator, between the junction and the bottom of the speaker cone, also does not show

up in the TF data.

4.2. B&K pinhole dataset

In section 4.1, it is suggested that the proposed method might be better suited to deal with real spurious resonance, which is situated at a distinctly different frequency from the actual resonance of the probe. To confirm this, experimental calibration data are considered in this section. The simplest probe TF to model is that of a pinhole backed by a microphone with a 'flat' TF. With this term, one refers to the amplification being close to unity within the desired frequency range and, possibly, a phase close to zero.

The TF of a pinhole probe is well documented, containing either line or cavity resonance of the form shown in fig. 1.1. Only a single resonant frequency at 5.5 kHz in fig. 4.3 shows a $-\pi$ rad phase shift accompanied by a resonant amplification peak. Hence, this resonance is deemed physical and part of the pinhole probe TF. Numerous secondary resonant peaks appear to be present at 1 kHz, 3–5 kHz, and 6–10 kHz. Nevertheless, the results of this dataset are also strongly dependent on the settings used for the BI, i.e., the defined prior PDF and data variance, and the preprocessing of the data provided to the method. By band-removing parts of the TF that are deemed to contain spurious resonance, e.g., because they deviate from the canonical TF of the probe, the proposed optimal fit α_{MAP} can change.

Hence, three possible model fits are presented in fig. 4.3. Concerning fig. 4.3a, when the likelihood is relatively unrestricted, the fit will evolve towards a very high-viscosity solution. This is caused by the method struggling to differentiate between the true frequency response of the system and spurious resonance. Thus far, it has been assumed that spurious resonance would be randomly distributed in the TF. As such, the method would not be able to improve the mean deviation of the model TF to the true response and all the spurious resonance by skewing the fit. When the fit is restricted to frequency bands that are deemed to be relatively unaffected by spurious resonance, such as the clean resonant phase shift around 5.5 kHz or the high frequencies above 10 kHz, an improved model fit to the data in the resonant phase shift and the very high frequencies is achieved. This solution corresponds to MAPs with a lower viscosity than the initial fitting solution, i.e., characterized by larger $|\alpha|$. The decrease in viscosity is clear from the resonance, with the resonant amplitude peak becoming larger and the phase shift slope becoming steeper. These new MAPs are also closer to the initial guess, based on the estimated pinhole radius and the viscosity according to the international standard atmosphere. Compared to the $\overline{\alpha}_{\text{MAP}}$ of the unrestricted model fitting, the results of both fig. 4.3b and fig. 4.3c, where only the narrow region around 5.5 kHz in the TF phase plot is accounted for in the fit, are deemed more physically correct. Naturally, the plausible range of parameters can also be enforced by tuning the prior PDF. However, this demonstrates again the power of band-passing as a preprocessing method for the calibration data with regard to research question 4.

Logically speaking, the correct prior PDF is based on repeated measurements of the probe geometry or manufacturing tolerances. Similarly, for the likelihood, repeated calibrations of one probe can show the calibration data variance. The amount to which the final fitting solution u is allowed to differ from the data d is impacted by the measurement variance σ_d. Conversely, the amount to which the final parameter values $\overline{\alpha}_{\text{MAP}}$ are allowed to differ from the initial guess $\overline{\alpha}_0$ is impacted by the prior PDF variance. A better fitting solution might be reached with parameters further from the initial guess, thus, the variance from the prior and likelihood have a combined impact on the posterior. Previous calibration repeatability studies showed a data variance for $|TF|$ in the range of 1×10^{-8} to 1×10^{-3}, and for $\angle TF$ in the range of 1×10^{-6} rad to 1×10^{-2} rad. Compared to the example variance of the calibration data, the prior PDF variance can be much larger. As a result, the prior will have little effect on the posterior, and the likelihood is allowed to pull parameters to possibly questionable values. The closed form of the posterior for linear models in eq. (2.10) shows how, even for non-linear models, both variances impact the final posterior variance and MAP. For this reason, manual tweaking of the measurement variance and prior is advised. In part, it also answers research question 5. The impact of the chosen prior and data variance depend on each other and the specific model. An example of the effect on the posterior by using a different prior for $|\alpha_{\text{side}}|$ can be observed by comparing the more narrow contour of fig. 4.4c with that of fig. 4.4b. The credible region of the posterior PDF is directly influenced by the uncertainty linked to the data, i.e., σ_d, and the uncertainty linked to the parameter values, i.e., the variance of the prior PDF.

In regards to the prior, accurate measurements of the probe geometry, i.e., tube lengths and radii

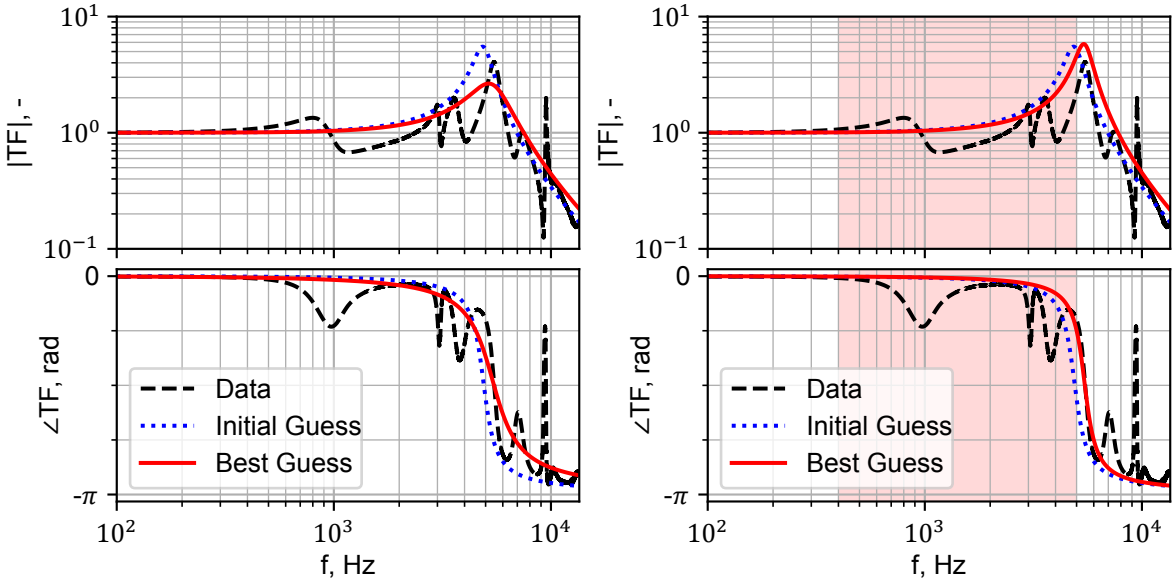

(a) Complete frequency range, $f \in [0.1, 13.5]$ kHz.

(b) Band-passed, $f \in \{[0.1, 0.4], [5, 6]\}$ kHz.

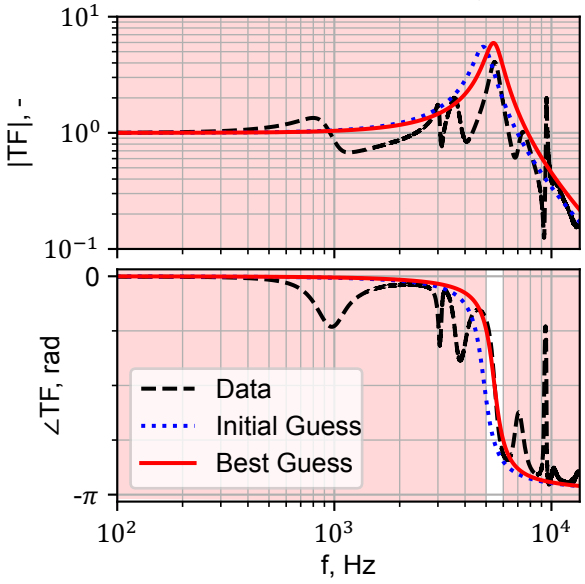

(c) Band-passed, $f \in [5, 6]$ kHz.

Figure 4.3: $TF_{flush \to pinhole}$. The red-tinted regions denote band-removed frequency bands.

and transducer cavity volumes, are possible albeit involved [9]. Using simpler measurement techniques such as calipers, cavity volumes hold the strongest uncertainty. They include not only the cavity in which the microphone sits but also the volume between the frontal surface of the microphone protective grid and the microphone membrane. Therefore, in general, it is sound to define a larger uncertainty, therefore, the prior PDF variance, for (V_v/V_t) than for the other geometric parameters.

Compared to current manual processing techniques that do not involve modeling the probe, the operator dependence on the results is much lower. More importantly, the frequency band affected by spurious resonance is reconstructed following the physics of the model. Comparatively, manual processing techniques tend to replace affected frequency bands by smoothing the combined TF from different calibrations and/or interpolating the surrounding correct TF data. Even when using a fraction of the available calibration data, such as in fig. 4.3c, a physically-correct calibration can still be achieved.

A major problem raised by this dataset is how to determine the correctness of the MAP. Three possible MAPs are presented for this dataset, but no objective metric with which they can be graded is presented. Depending on the goals of the experimental campaign, different pressure-measurement met-

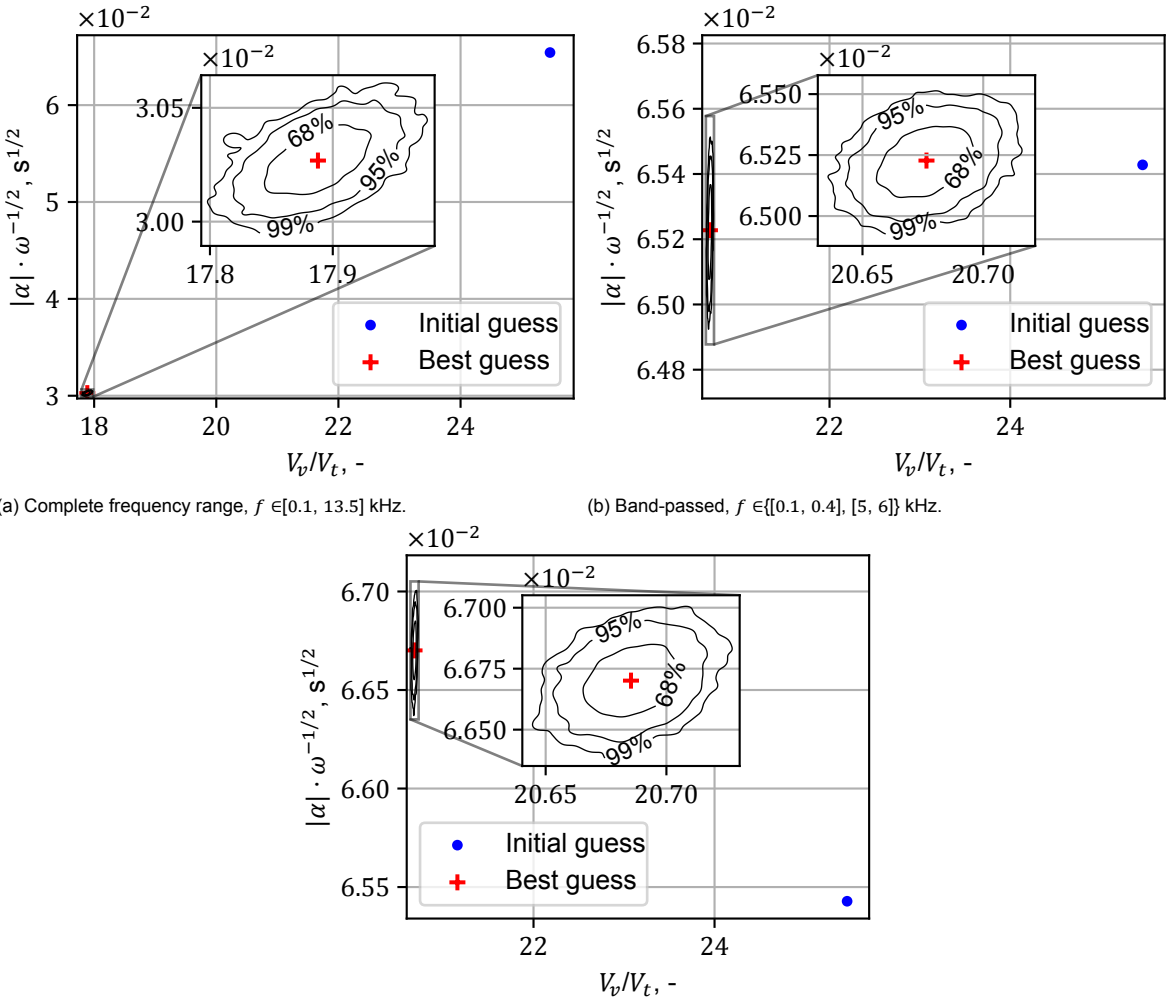

(a) Complete frequency range, $f \in [0.1, 13.5]$ kHz.

(b) Band-passed, $f \in \{[0.1, 0.4], [5, 6]\}$ kHz.

(c) Band-passed, $f \in [5, 6]$ kHz.

Figure 4.4: KDE of posterior samples linked to McMC in fig. 4.3.

rics are of interest. For example, in aeroacoustics, WPS can be used to analyze the noise-production mechanisms due to pressure fluctuations on the surface of a body submerged in flow [6] or its trailing edge [7]. These experimental investigations typically include a benchmark case to which new configurations are compared, or that is used to validate the experimental setup against preexisting data or theory. Although the present benchmark data, e.g., a ZPG flat-plate TBL WPS, can be compared against prior data or the theory [19] as a metric for the accuracy of the calibration, no wall-pressure measurements exist for the B&K pinhole probe of this dataset.

4.3. Electret pinhole dataset

The dataset presented in this section does offer such reference measurements, which can be used to evaluate (i) how close the calibration can get the measured WPS data to the theory and (ii) how much can be gained by using an improved method for removing spurious resonance from calibration data. The distinctly non-'flat' frequency response of the electret microphone used in the pinhole does represent an issue with the semi-empirical calibration method. The method fits an analytical model for the frequency response to the calibration data, which includes the TFs of the microphones along the calibration chain. The analytical model only considers the viscous and resonance effects within the tube-cavity system, therefore not the TFs of the microphones. A separate empirical model needs to be provided to account for the characteristic TF of the electret microphone.

The dataset of the pinhole electret calibration, unsteady wall-pressure measurements, and the flush-mounted electret frequency response data presented in this section are from previous unpublished

experiments performed at the VKI. A simple parametric model that covers the full range of possible flush-mounted electret TFs is shown in fig. 4.5 with a minimal amount of parameters. More parameters decrease the convergence rate of the McMC, and too much freedom in the achievable states of the empirical microphone TF model might cause an overlap with the parameters of the tube-cavity system model, leading to a range of MAP.

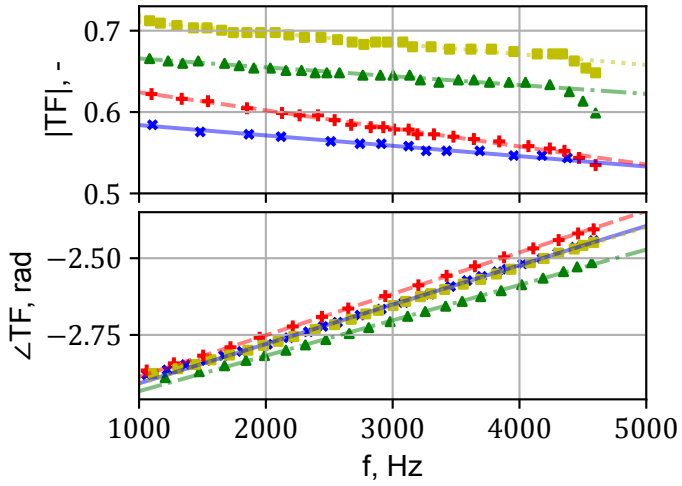

Figure 4.5: Calibration data from various electret microphones. The markers indicate the available data, the lines indicate a linear regression of the data. This linear regression represents the simplest empirical electret model.

Incidentally, the calibration data of various flush-mounted electret microphones in fig. 4.5 can all be easily represented by first-order polynomials for both the amplitude and phase of the TFs. In total, such a model has 4 parameters. A strong correlation between parameters would allow the number of effective parameters to be reduced. More calibrations of the similar flush-mounted electret microphones should shed light on the plausible ranges for the model parameters, which would be helpful in defining the prior PDF of these model parameters. The amplitude intercept of the electret model used for the fit in fig. 4.6 differs from those presented in fig. 4.5, in part because the pinhole calibration data are already corrected with the measured microphone sensitivity.

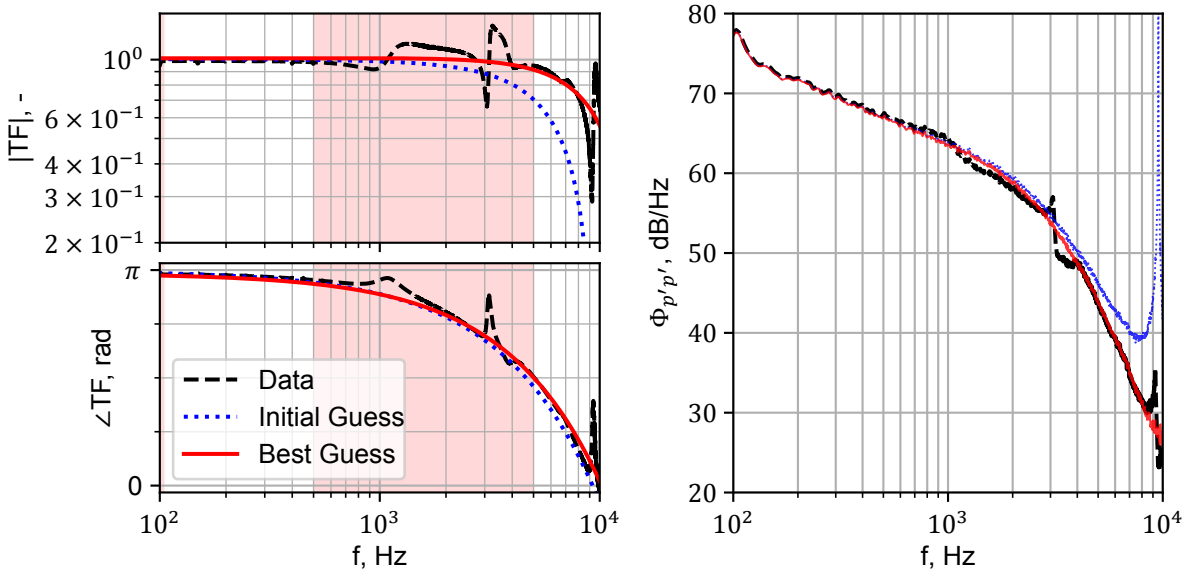

(a) $\mathrm{TF}_{\mathrm{ref.}\to\mathrm{pin.}}$ calibration data.

(b) WPS for $U_\infty = 19.7\,\mathrm{m\,s^{-1}}$.

Figure 4.6: Pinhole electret TF and WPS data referred to a ZPG TBL flow. The red-tinted regions denote band-removed frequency bands.

The calibration data depicted in fig. 4.6a does not show the expected pinhole frequency response,

with either clear cavity or line resonance. The amplitude slowly decays from 3 kHz onward, without any resonant peak in the amplitude of the TF beforehand, such as in fig. 1.1. The phase does not exhibit a sudden resonant shift but only the linear response expected from the electret. It is, therefore, theorized that the resonant linked to the cavity lies above the considered frequency range and that the TF within the calibrated frequency range is only affected by the frequency response of the electret microphone. Therefore, only the empirical electret model is used for the fitting of this dataset. The quadratic decay in amplitude must then be part of the electret TF, for which no data in fig. 4.5 are available at these high frequencies. As such, a polynomial of second order is required for the amplitude of the model electret TF. The final model for the electret transducer is shown in eq. (4.1). For pinholes with larger V_v/V_t, a combination of both analytical and empirical transducer models could be effectively used, showing the flexibility of the method to the specificity of the considered dataset.

$$|TF|_{ele.}(f) = a_{|TF|} \cdot f^2 + b_{|TF|} \cdot f + c_{|TF|} \qquad \angle TF_{ele.}(f) = a_{\angle TF} \cdot f + b_{\angle TF} \tag{4.1}$$

The WPS of fig. 4.6b result from unsteady ZPG wall-pressure measurements corrected with the inverse of the different calibrations shown in fig. 4.6a, i.e., pinhole to reference microphone. The spurious resonance at 3.3 kHz and 10 kHz is apparent at first glance. More interesting is the 0.5 kHz to 3 kHz range, which is smoothened by the proposed method. The more gradual decrease in WPS that results from the considered calibration method is deemed to be closer to canonical ZPG TBL WPS, as would result from the model of Goody [19]. Whereas these first two resonant frequencies can be removed with manual post-processing, a method without an underlying model for the TF can not bridge the large frequency band in a correct way. In particular, when this frequency band is affected by attenuation or resonance linked to the tube-cavity geometry, only a model-driven method such as the proposed one would be able to adequately correct the calibration data.

Finally, considering the posterior PDF in fig. 4.7, several parameters are strongly correlated. Hence, the prior will have a strong impact on the MAP. A wrong prior might result in a wrong MAP while still achieving a very good TF fit. If removing spurious resonance is the only goal, then this poses no issue. However, the credible region might not reflect the uncertainty linked to the calibration very well. Additionally, in case geometrical parameters such as V_v/V_t were to be used, a wrong MAP cannot be used to apply accurate corrections to the calibration of the probe.

Nevertheless, the main objective here is the development of a method for removing spurious resonance from empirical calibration data in a way that is less influenced by the operator. The successful TF fit with the combination of the empirical electret model shows, once again, the range of cases for which the proposed method returns usable results. And the plausible combination of various models for fitting, such as the W model and the presented empirical electret model, highlights the flexibility of the method. Observing the WPS in fig. 4.6b, the advantage of the proposed method over current processing methods is clear. The absolute error in the pressure-derived quantity made by spurious resonance in the calibration is case-dependent. The error in WPS is considered as the difference between the WPS with an uncorrected TF with respect to the TF corrected with the proposed method. For this dataset, errors at three frequency bands are observed: two narrow bands of 4 dB error at 3 kHz and 9 kHz, and a longer frequency band with an error in the range of 1 dB from 0.5 kHz to 3 kHz.

A more accurate evaluation of the error of the method might be a comparison of the ZPG TBL WPS with the results of the model of Goody [19]. For this, several boundary-layer parameters are required, which are unavailable for this dataset. With the aim of presenting a dataset with this more objective determination of error and displaying the usage of the proposed method, a new measurement campaign is performed. The results are presented in section 4.5. However, the underlying analytic W model can also be used for the design of the RMP to be employed in the experimental campaign. The findings of this parametric study, aimed at answering research question 2, are discussed in section 4.4.

4.4. Probe Design

The specific needs of an experimental campaign can impose requirements on the microphone probes that are used. Pinhole-type RMPs are frequently used, as the reduced sensing size and possible decreased distance between probes are well-known advantages. However, some experiments might require the transducers to be mounted further away from the sensing area of the probe.

In the design of RMPs, the goal is often to have as little impact on the total system TF as possible, i.e., have a 'flat' TF. Therefore, the goal is often to move resonant frequencies outside the frequency

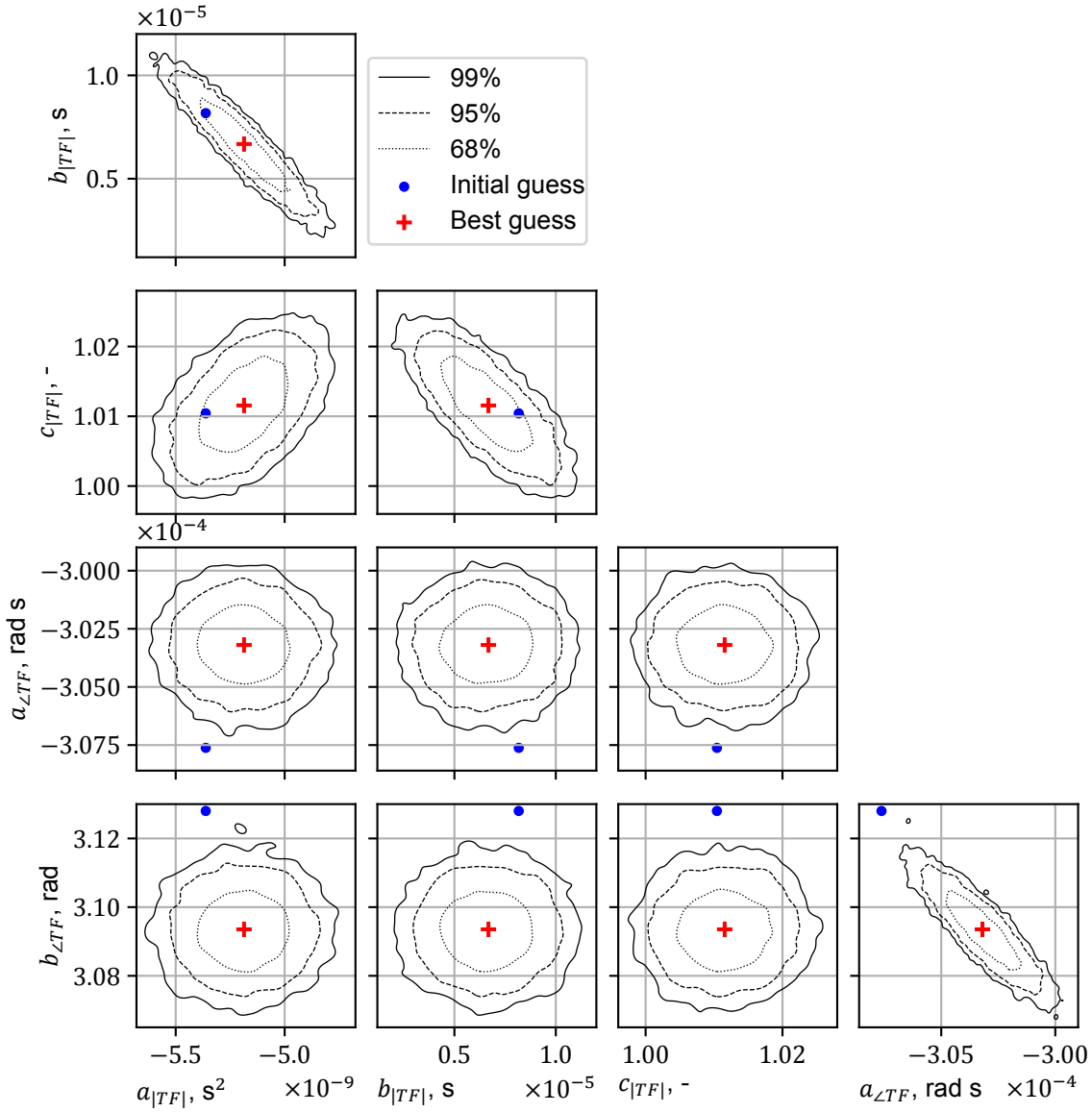

Figure 4.7: KDE linked to electret pinhole McMC in fig. 4.6.

band of interest and minimize viscous attenuation. Resonance amplifies the frequency components of the pressure-fluctuation signal that are close to the resonant frequency. If a loud signal is acquired, this resonant amplification might saturate the microphone. The opposite can also be undesirable, as viscous attenuation can remove a large part of the energy of the signal acquired by the microphone. Background noise acquired by the microphone that does not enter the RMP inlet, or electronic noise, might start to dominate the useful signal in parts of the frequency range. In both cases, the TF of the probe, estimated through calibration, corrects for the attenuation or amplification. However, the further the TF is from being 'flat', the larger the impact of the TF on the final TF-corrected unsteady pressure measurements will be. Any calibration error is amplified the larger the impact of the TF is.

For example, in fig. 3.3a, to minimize the intrusivity of the probe on flow inside of the porous liner, all voluminous parts of the probe should be mounted below the liner with only a thin capillary tube sticking through the liner. If a pinhole probe were to be used, the minimum line distance would be the thickness of the liner plus some possible length for a solid plate below the liner and the mounting solution of the microphone, i.e., ca.26 mm. For a short pinhole probe, it should be possible to achieve a TF with the most resonant frequencies outside the frequency range of interest. A single cavity-resonant frequency might be present, following eq. (2.6). However, for a long pinhole, additional line resonance and its modes are inevitable (see eq. (2.5)).

Using a semi-infinite waveguide type RMP, referred to as 'RMP' for conciseness, the same design requirements can be fulfilled with strongly reduced line resonance strength. The geometry is further explained in section 3.4, and visualized in fig. 3.3b. The response of both probes is compared in fig. 4.8a.

It is believed that semi-infinite waveguide RMPs can be designed for the specific needs of any measurement campaign. The RMP features the same low intrusivity as a pinhole. However, RMP can be designed to be easily removed in its entirety from the model it sits in. For example, the RMP in fig. 3.3 can be removed from the porous liner, capillary tube included, without needing to remove the liner from the wind tunnel. The RMP can then be calibrated in a solid-walled calibration jig. In contrast, low-intrusivity pinholes might need to be permanently built into a porous airfoil. Such a configuration requires in-situ calibration of the probes, i.e., by placing the calibrator on top of a porous surface containing the pinhole probe. In such a case, it is impossible to match the pressure field inside of the calibrator over both calibration steps, as the porous surface does not properly seal the calibrator. Therefore, a single-step calibration method would be needed. Research sub-objectives 3 and 4 and the accompanying research questions 9 and 11 were aimed at investigating a possible solution to the problem of porous in-situ calibration by using the proposed semi-empirical calibration method. However, the ease of calibration offered by the semi-infinite waveguide RMP means that accurate calibrations can be achieved without the need for correcting calibration data from a flawed calibration setup. Therefore, the efforts of this project were diverted to the other aspects of the problem.

The mounting of the side branch to the main channel and the side branch itself increases the tube length between the sensing area and the microphone of the RMP, compared to a pinhole. Hence, there is more viscous attenuation for the RMP than for the pinhole probe. However, compared to the pinhole, only the transducer-cavity resonance at ca. 1.8 kHz remains. As such, this probe design is much better suited for acquiring flows that would otherwise saturate the microphone. Viscous attenuation can also be leveraged as an advantage in the design of the probe to counteract possible foreseen saturation.

The main design limitation of the RMP in this experimental campaign is the tube length of the upper element before the side branch. The minimum length is linked to the thickness of the porous liner. As shown in fig. 4.8b, a shorter length reduces viscous attenuation, but a longer line can be used to resolve the potential saturation of the microphone during the experiment. Naturally, the radius of the main tube in fig. 4.8c has a similar attenuating effect. Here, the radii of the tube sections before and after the side branch are changed simultaneously, as any discontinuity in radius would result in line resonance linked to the length of the separate sections. Therefore, making sure that there are no discontinuities in the main channel of the probe is crucial during production.

The exact goal of the long tube after the RMP side branch, i.e., the attenuation tube, is to have as little resonance linked to the main tube as possible. In this regard, an important parameter to get right is its length. Indeed, the tube should be long enough that little-to-no pressure waves that reach its end are reflected back to the RMP side branch and picked up again by the microphone. As shown in fig. 4.8d, the lowest frequency waves are the least susceptible to viscous attenuation, and, therefore, dictate the required line length. The W model can be effortlessly used to find the minimum required length.

A strength of using analytic models such as the W model for the design of the RMP is that it can be tuned for the specific conditions that it will see during the measurements. Understanding the impact of the conditions can therefore be important. An increase in temperature during the measurements with respect to the conditions during calibration will tend to push all resonant frequencies higher. The result presented in fig. 4.9a is a combination of two effects. The change in speed of sound with flow temperature will increase the resonant frequencies but also increase the strength of the resonance, in both amplitude and phase. However, the increase in viscosity with temperature will bring the resonance strength back to a similar level. Instead, the effect of grazing flow over the orifice of the RMP seemingly attenuates the incoming pressure waves, which can be helpful as high-velocity flow might also result in larger pressure fluctuations that might otherwise saturate the microphones. Naturally, with increasing velocity, the attenuating effect becomes more pronounced.

Crucial is that the impact of temperature and grazing flow on a probe with pronounced resonance, such as fig. 4.10. With an increase in temperature, the resonant peak in $|TF|$ shifts to another frequency. The pressure signal at the old resonant frequency will be attenuated with a factor close to the magnitude of the resonant amplitude peak, while the pressure signals that are amplified by the actual shifted resonance of the probe will not be corrected. For grazing velocity, as it is evident from comparing

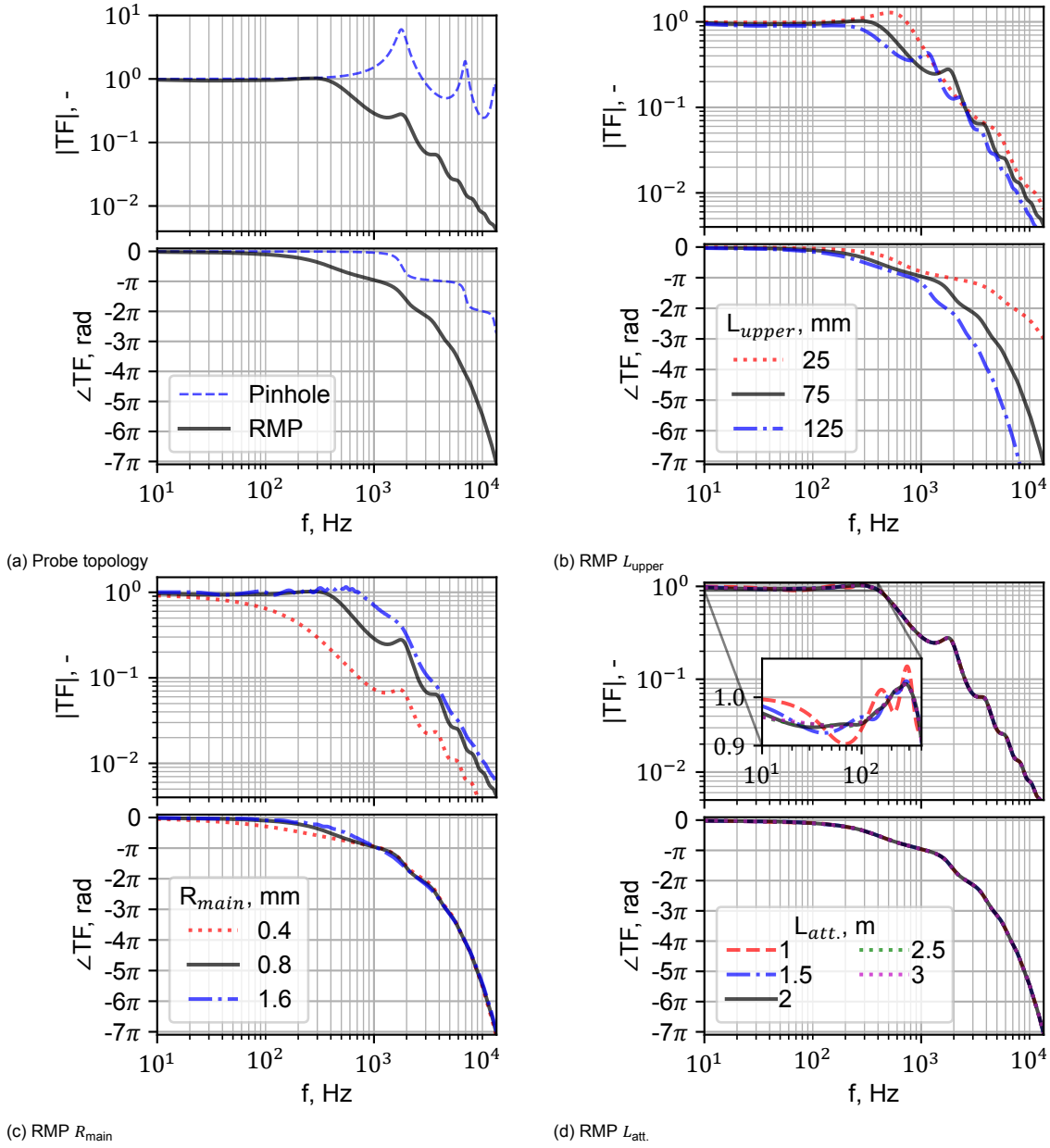

(a) Probe topology

(b) RMP L_{upper}

(c) RMP R_{main}

(d) RMP $L_{\text{att.}}$

Figure 4.8: RMP parameter effect on TF. Probe geometry shown in fig. 3.3b used as a reference (black line).

fig. 4.10b with fig. 4.9b, the stronger the resonance, the more this is attenuated by the grazing flow. Hence, not accounting for this effect in the TF of the probe results in larger errors when the probe already exhibits strong resonance in still-air calibration conditions.

Further testing with the grazing-flow model is required to provide a useful answer to research question 6. While, in general, any remaining resonance in the RMP appears to be attenuated, there is the possibility that the complex RMP has its TF affected in other ways too, e.g., in a way that amplifies certain frequencies. However, to currently apply the grazing flow correction, a single tube-cavity element of Bergh and Tijdeman [9] needs to be inserted at the inlet of the RMP, while the branching RMP itself requires the W model. As such, the combination of tube cavities of both of these models appears to result in problematic results in some of the tested cases. The development of a better link between the analytic model for branching RMP topologies and a grazing flow correction model [5, 11] is an ongoing investigation. With the improved grazing flow correction implementation for branching pneumatic systems, a better understanding of this specific effect can be gained.

In conclusion, semi-infinite waveguide-type RMPs can be tweaked to provide a measurement in-

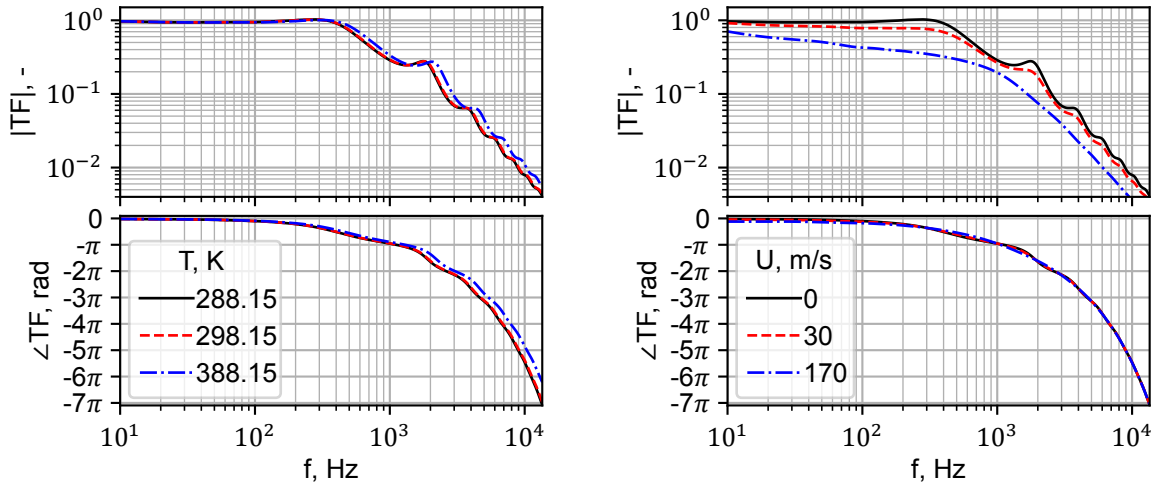

(a) RMP temperature.

(b) RMP grazing flow.

Figure 4.9: RMP effect of flow mean temperature and grazing flow velocity [11] on TF. The probe geometry is shown in fig. 3.3b.

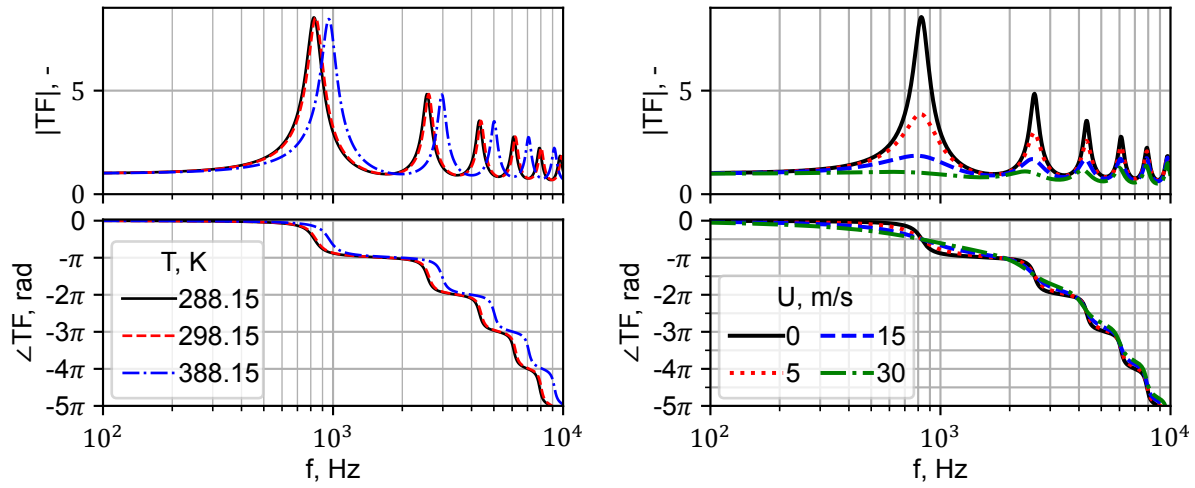

(a) Pinhole temperature.

(b) Pinhole grazing flow.

Figure 4.10: Pinhole effect of flow mean temperature and grazing flow velocity [11] on TF. $(L, R, V) = (90\,\text{mm}, 1.5\,\text{mm}, 10\,\text{mm}^3)$.

strument that fits the exact needs of the experiment. However, due to the many parameters, the design of these probes requires more investigation than simple pinhole probes. This is where analytic models such as the W model can be exploited. A highly accurate prediction of the TF is returned with little computational effort, enabling one to rapidly iterate designs. As such, the TF can be tuned, even considering the impact of the mean temperature, pressure, or grazing flow that will affect the probe during the measurements.

4.5. RMP dataset

The final dataset came to be due to (i) the need for a dataset that contains not only microphone calibrations and unsteady wall-pressure measurements but also the boundary-layer parameters linked to the wall-pressure measurements and (ii) the need for WPS and boundary-layer velocity measurements over a porous wall-insert, as a validation dataset for another project. A semi-infinite waveguide type RMP is designed for this campaign, as it minimizes the intrusivity of the probe on the flow through the porous liner. The design of such RMP probe is further discussed in section 4.4. While such a RMP topology has fewer internal reflections than a pinhole of an equivalent length, the complexity of the TF is not trivial compared to the short pinholes of the prior datasets. The geometry of the RMP is also more complex than the pinhole, using more parameters in the fitting process. For this reason, the RMP

is presented as the final and most complex dataset.

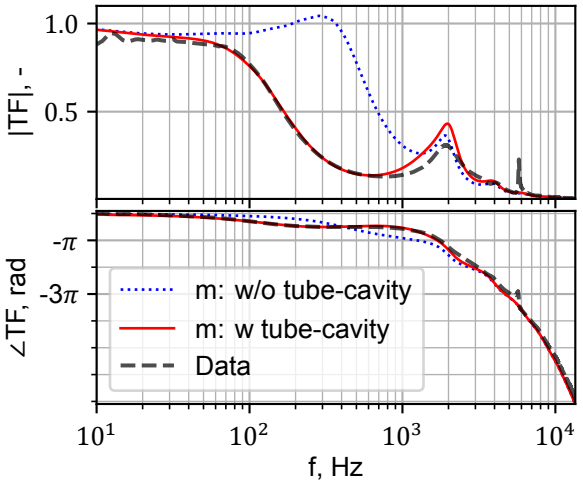

(a) $TF_{ref.\rightarrow RMP}$ of RMP with and without additional tube-cavity in model geometry. In the legend, 'm' denotes the W model TF.

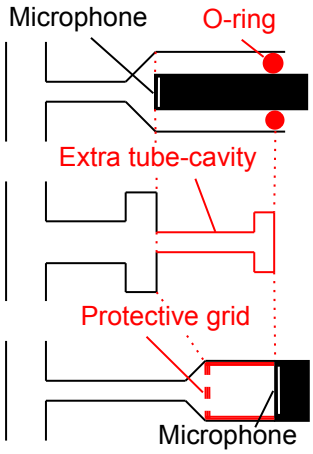

(b) Schematic of the extra tube-cavity modeled in the system. The leakage and protective-grid hypotheses are shown.

Figure 4.11: RMP calibration data with W model fit, and WPS acquired with said probe and calibrated with the data and W model TFs.

Initial attempts to apply the proposed semi-empirical calibration technique on the RMP calibration data do not result in satisfactory fits, e.g., the model fit in fig. 4.11a without the tube-cavity. The calibration data fall outside of the scope of achievable model states. While the W model may be suspected, it did not present an issue for the FEM RMP in section 4.1 nor the calibration data in the source document of the model [10]. Assessing the correctness of the TF of a RMP is difficult since the TF of most RMP is simply less documented than that of a pinhole. The underlying W model can be exploited here to investigate the impact of possible changes in the model geometry on the TF, e.g., by adding tube-cavity elements where possible discontinuities may appear.

Notably, a good fit between the model and RMP calibration data is found when an extra tube-cavity element is added in series after that of the RMP side-branch, as shown in fig. 4.11. This finding leads to two hypotheses, both schematized in fig. 4.11b: (i) the possible existence of a leak in the current clamping method of the microphones, or (ii) the impact of the protective grid, which acts as a discontinuity. Further testing is required to ascertain the source of the additional resonance. Regardless of the source of this effect, it is evident that it can be modeled well as an extra tube-cavity element using an effective radius. Since all wall-pressure measurements are acquired with these probes, all presented fits contain the extra tube-cavity geometry. The canonical nature of WPS can be used to show that the extra tube-cavity geometry is part of the probe, as not accounting for it properly in the model would not lead to the expected trend. The WPS resulting from the RMP can be seen in fig. 4.12b, which presents only the frequency range not contaminated by background noise. The measured spectra are corrected for averaging small wavelengths related to the finite sensing area of the RMP, using the model of Corcos [8].

With a RMP such as this one, more fitting parameters are present than for a pinhole: 12 and 2 parameters, respectively. If a wrong variance is chosen for one of the axes of the sampling PDF, it affects the performance of the overall chain. More parameters make the debugging harder. As with section 4.1, the underlying model is used to analyze the effect of separate parameters and narrow down the number of fitting parameters.

Taking into account the added difficulties of the many model parameters, the current fit presented in fig. 4.12 is not optimal. Indeed, with the current sampling distribution variance, the correlation between samples is too large to provide a useful KDE, and a better MAP is possibly still achievable. Compared to fig. 4.11a, a logarithmic scale is used for the amplitude to be able to more easily visualize the differences between the model TF and calibration data over the entire frequency spectrum, i.e., including the high frequencies where the amplitudes become very small. It is believed that with more time and BI-related knowledge, more optimal McMC parameters could be found, leading to a closer fit of the W model to the RMP TF data. In fig. 4.12a, the high frequencies above the 2 kHz RMP transducer-cavity resonance

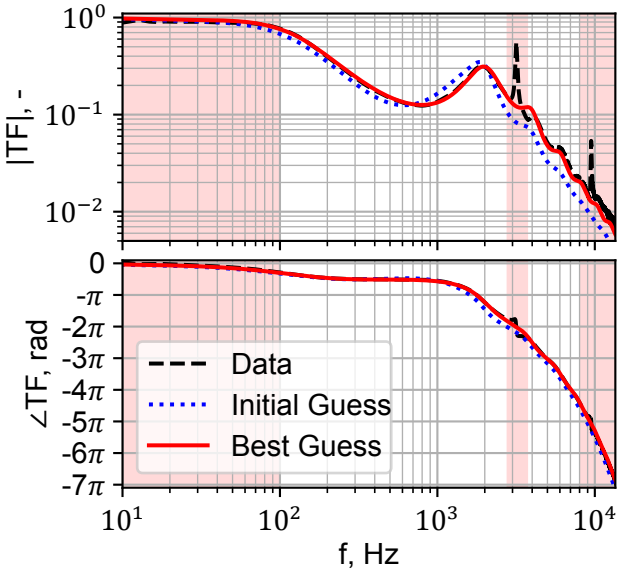

(a) RMP $TF_{ref.\rightarrow RMP}$ data and W model fit.

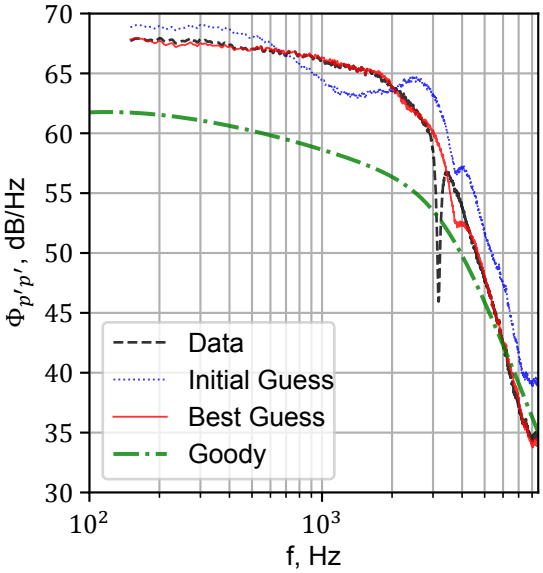

(b) WPS acquired with RMP with an outer flow velocity of $U_e = 19.7\,\mathrm{m\,s^{-1}}$. RMP positioned at $x/L = -0.33$ in fig. 3.3a.

Figure 4.12: RMP calibration data with W model fit, and WPS acquired with said probe and calibrated with the data and W model TFs. The Goody model WPS uses the parameters from table 1.

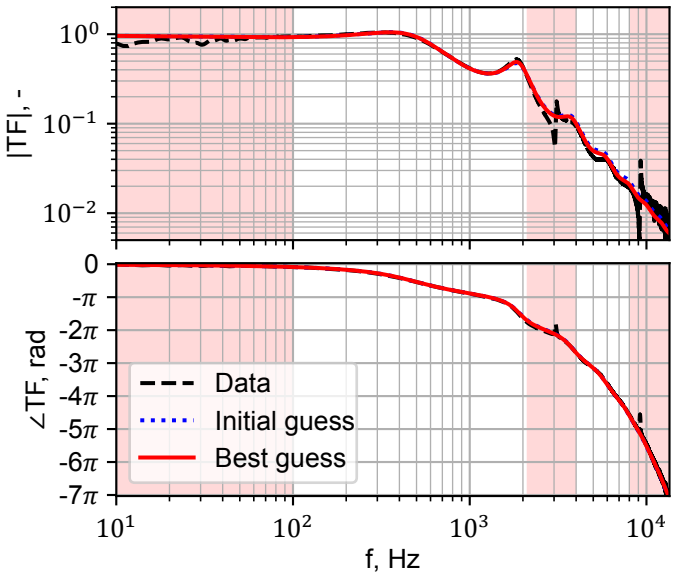

Figure 4.13: RMP $TF_{ref.\rightarrow RMP}$ calibration data, which are not affected by the 'extra tube-cavity element', and W model fit.

contain several resonant peaks. This resonance appears to be largely created by the line discontinuity of the extra element cavity with respect to the RMP side-branch tube cavity. Nevertheless, while the 4 kHz imperfection of the TF fit propagates into the WPS, the 2 kHz spurious resonances in both TF and WPS are successfully removed.

The correction for sensing-area averaging of Corcos [8] helps bring the high-frequency slope of the WPS closer to the theoretically correct slope of Goody. A large difference of ca. 6 dB is still present between the theoretical WPS and the measured one. From preliminary analysis with the model of Tijdeman and Bergh [11], it is believed that the effect of grazing flow forms part of this discrepancy. As mentioned in section 4.4, the current implementation of this correction needs further testing. Therefore, the goal of using it to reduce the deviation between the model and the data, i.e., research sub-objective 1, could not be fully realized yet. The implementation of a working grazing-flow correction will make it

possible to achieve this objective. And, due to the $\overline{\alpha}_{MAP}$ being found in the model fit, applying corrective terms to the TF is almost effortless.

Later testing managed to provide RMP calibration data without the aforementioned 'extra tube-cavity element' effect, confirming that the W model is capable of predicting the TF of such branching probes (fig. 4.13). However, no unsteady wall-pressure measurements are available for this RMP calibration. Without the extra tube-cavity system, three less fitting parameters are required to apply the technique to the RMP calibration data, substantially reducing its computational cost. Although more time and tuning of the sampling distribution variance are still required to improve the fit, these results demonstrate that the method presented in this chapter can successfully deal with complex RMP geometries.

In summary, the proposed semi-empirical approach for RMP calibration does take some initial time investment in setup for the specific pressure probe when compared to the current manual post-processing approaches involving splicing and smoothing the calibration data. However, compared to the manual processing method, the novel method aids the user in understanding which resonance is physical to the probe and which is calibration-induced. Any spurious resonance in the TF is corrected by this approach using the fluid-dynamical physics of the underlying model. Especially for wide frequency bands affected by spurious resonance, e.g., $f = 0.5 - 3\,\text{kHz}$ in fig. 4.6, the method can yield results that are simply unachievable by manual processing using interpolation of the surrounding frequency bands or similar approaches.

Several research avenues remain open for further work. One such promising idea is to correct for the difference in mean temperature and pressure experienced by the RMP between calibration and measurements. Much like grazing flow, temperature and pressure have an impact on the TF of the probe, as discussed in section 4.4. However, for the experiments performed in this research project, where the only temperature changes are atmospheric in nature, the largest differences in temperature are in the range of $10\,\text{K}$. For temperature differences of this order, the impact on the TF is simply too small to be observed or corrected in the calibration data. And for such a small impact on the TF, the linearization of the model has little influence on the accuracy of its results, as asked in research question 7. Comparing both effects in fig. 4.9, it is clear that the grazing flow has a much larger impact at the flow velocities and temperatures considered in the presented measurements. The idea behind research sub-objective 2 and research question 8 remains a very interesting one. But the true value of it might only be evident for experiments with a large temperature difference to the calibration conditions, e.g., high temperature due to combustion [13].

5

Conclusion

The main objective of this investigation is to develop a method for removing spurious resonance from empirical calibration data of microphone probes. The proposed semi-empirical calibration method achieves this goal by fitting an existing model for the frequency response of pneumatic systems to the calibration data using Bayesian inference. In doing so, all probe-induced resonance is represented in the model response, and the resonance that cannot be produced by the considered probe and physics, i.e., the spurious resonance, is ignored and removed.

The method is successfully applied to several datasets, ranging from an inviscid FEM simulation to real plane-wave tube calibration data of pinholes with varying microphones and more complex RMP. Each dataset presents different strengths and limitations linked to the proposed method. Most impressively, the technique replaces the frequency bands affected by spurious resonance with a physics-based alternative. The uncertainty of the model fit is quantifiable through the credible regions of the posterior PDF, which allows for uncertainty bounds to be propagated to the TF and pressure measurements.

The main limitation of the method is that there is still some operator intervention required in analyzing the results of the model fit on the data. In analyzing the fit, two possible caveats should be considered: over-smoothing of the fit and non-unique solutions. When the BI method converges to a local optimum, the lack in the quality of the fit can be quite apparent and indicates the need for some tweaking of the BI step size or initial guess. However, multiple parameter values that give equally satisfactory fits to the TF of the probe can not be apparent on a first inspection. Here, the more physically-correct parameter values need to be prioritized with the user-provided prior PDF. If the model geometry oversimplifies the real-life counterpart, some resonance will be considered spurious by the method, whereas it is physical, e.g., caused by a radius discontinuity of a tube. Manually playing with the topology of the probe and parameter initial guesses can shed light on whether or not such errors are being made.

In conclusion, in its current form, the proposed method delivers better results than the current manual post-processing methods. Yet, even more potential remains in the presented method: the MAP parameter values found during the fitting process can be effortlessly used as inputs to corrective models such as Corcos [8] and Tijdeman and Bergh [11]. The latter correction for grazing flow is especially helpful for high Mach-number flows, although preliminary testing shows that the impact might already be non-negligible for flows of $M = 0.1$. For high-temperature flows, the proposed method may also prove to be beneficial. The TF of the probe reflects the temperature and pressure during calibration. Using the model fit with the calibration data, it can be investigated whether changing the conditions to match the measurement ones in the model can appropriately represent the effects on the TF of the probe. For smaller temperature changes of ca. $10\,\mathrm{K}$, such as encountered by the change in atmospheric temperature, this effect is very small and hard to observe. Hence, in order to investigate the possible temperature-correcting capabilities of the proposed semi-empirical method, another experimental campaign is needed with much larger temperature differences, such as those encountered with combustion or high Mach-number flows.

Appendix: Investigation of a TBL over solid and porous liners

The aim of the experimental campaign presented in chapter 3 is to generate an accurate and extensive experimental dataset on the effect of porous liners on the TBL. This dataset consists of WPS and HWA measurements, detailed in section 3.4 and section 3.5, respectively. The velocity measurements are used to provide the streamwise evolution of vertical profiles of mean velocity, turbulent intensity (TI), and turbulent length scales. All measurements are performed at outer-flow velocities of $U_e = \{15\,\mathrm{m\,s^{-1}}, 20\,\mathrm{m\,s^{-1}}, 25\,\mathrm{m\,s^{-1}}\}$ and liners with cell-size $d_c = \{0\,\mathrm{mm}, 3.5\,\mathrm{mm}, 4.5\,\mathrm{mm}\}$. The $d_c = 0\,\mathrm{mm}$ refers to the solid plate, which serves as a reference, and more information on the porous liners and cell sizes can be found in section 3.5.

On the solid wall in fig. 1a, all BL profiles collapse well onto each other, indicating that no large streamwise pressure gradients are present. With the porous liners, i.e., fig. 1b and fig. 1c, there is a clear streamwise evolution of the BL velocity and TI close to the wall. The BL loses velocity close to the wall when flowing over the porous wall, affecting the shape factor of the BL. This is accompanied by an increase of TI close to the wall.

The wall-shear-stress-derived quantities provided in table 1, that are used for both the Corcos' correction and the Goody model WPS shown in section 4.5, are derived by fitting the velocity measurements onto a theoretical BL profile, as shown in fig. 2. Only the solid-wall results are presented, as no correct fitting can occur between the theoretical solid-wall ZPG BL model and the porous wall data.

Table 1: Boundary layer parameter of HWA profile at $x/L = -0.33$, used for the Goody model in section 4.5. Pressure normalized with ISA atmospheric sea level pressure, p_{atm}.

Parameters	Values	Parameters	Values
U_e, $\mathrm{m\,s^{-1}}$	19.7	H, -	1.36
δ, m	2.77E-2	u_τ, $\mathrm{m\,s^{-1}}$	7.55E-1
δ^*, m	4.71E-3	T, K	300
θ, m	3.47E-3	$p/p_{\mathrm{atm.}}$, -	9.93E-1

The WPS measurement results are presented in fig. 3. For the porous liner, the Corcos correction uses the wall-shear stress of the solid-walled case. The results for the microphones under the solid plate are not presented in fig. 3a, as they did not acquire any useful signal.

By using the W model for the design of the RMPs employed in this experimental campaign, as discussed in section 4.4, the intrusiveness of the probe to the internal flow of the porous liner could be minimized. The semi-infinite waveguide topology ensures that this low intrusivity does not come at the cost of an unfavorable RMP TF having strong resonance. The result in fig. 3 is a highly accurate WPS dataset, which uses the HWA data presented in fig. 1 to account for the attenuation linked to the sensing area size [8]. Further improvements to the proposed semi-empirical calibration method, in the form of the grazing-flow correction of Tijdeman and Bergh [11], are bound to yield even greater accuracy of the WPS in this dataset, which will be employed as a reference for the validation of porous models in numerical simulations by the partners of the INVENTOR project.

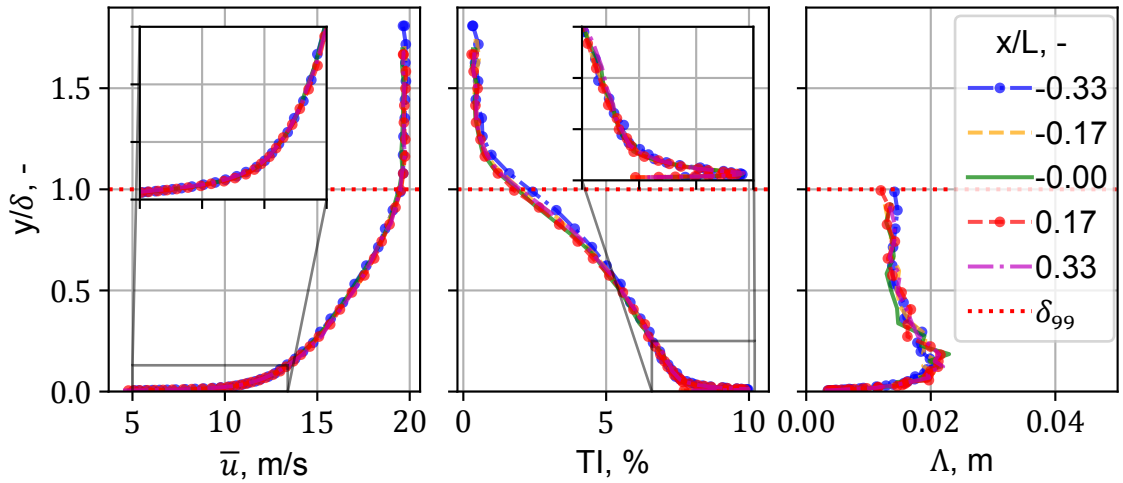

(a) Solid liner, $d_c = 0$ mm.

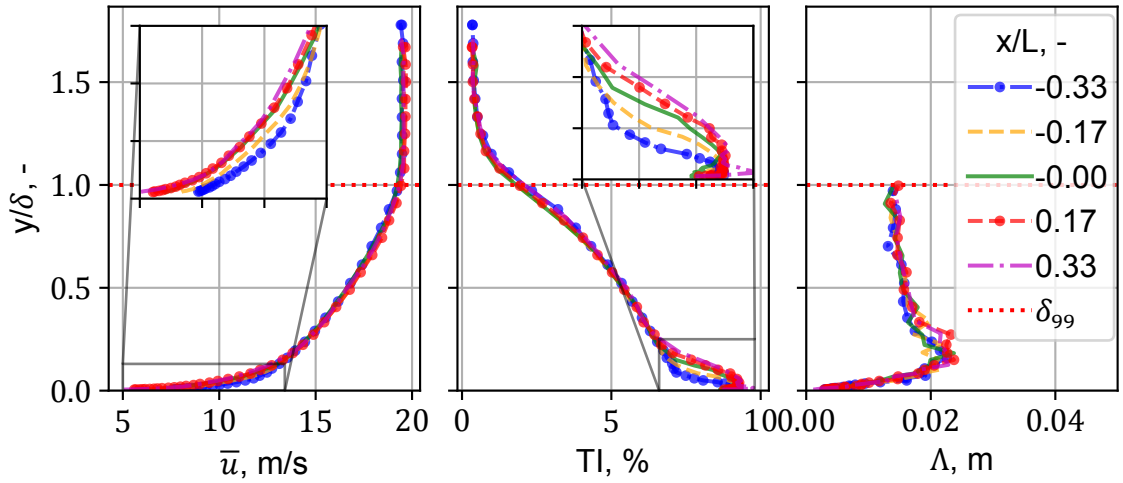

(b) Porous liner, $d_c = 3.5$ mm.

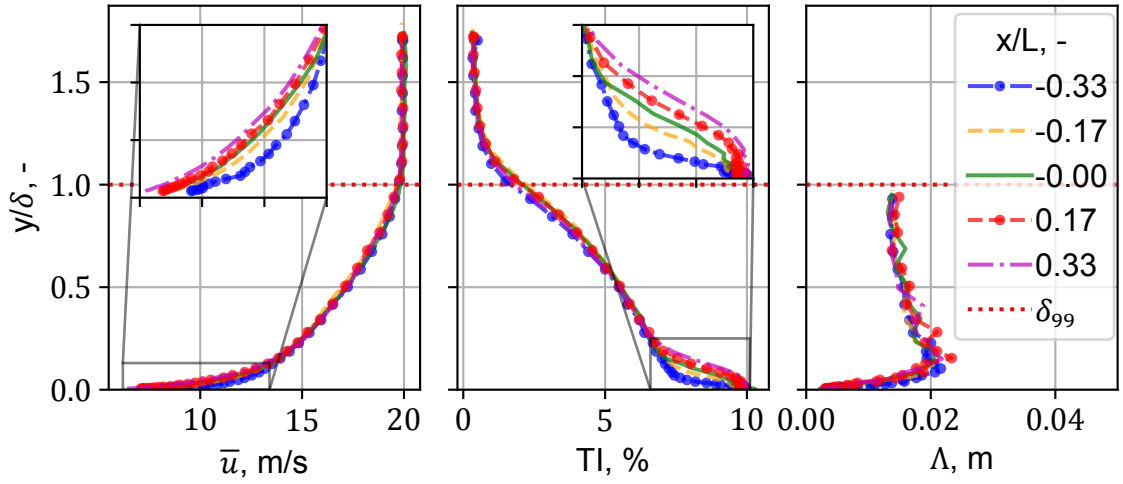

(c) Porous liner, $d_c = 4.5$ mm.

Figure 1: HWA measurements in station 2 at $U_e = 20\,\mathrm{m\,s^{-1}}$, for one solid and the two porous DMND liners with cell size d_c.

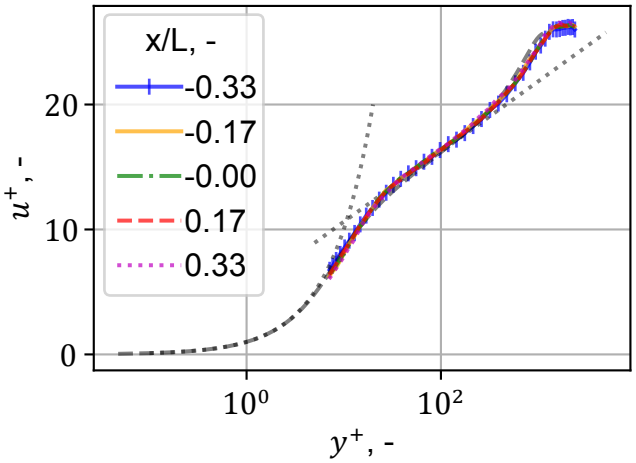

Figure 2: HWA BL profile in inner-wall units on a solid pate at $U_e = 20\,\mathrm{m\,s^{-1}}$. The dashed and the dotted black lines are theoretical ZPG BL profiles.

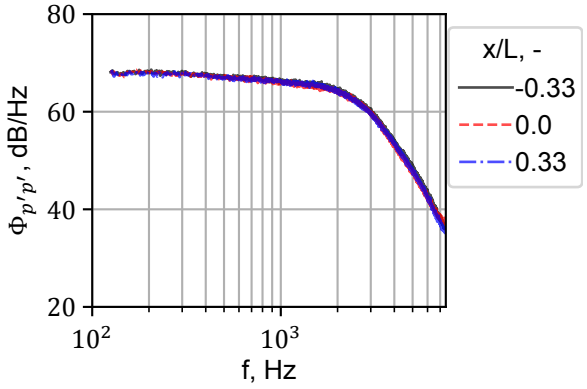

(a) Solid liner, $d_c = 0\,\mathrm{mm}$.

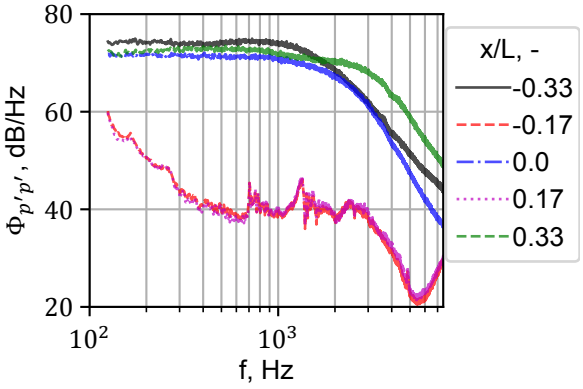

(b) Porous liner, $d_c = 3.5\,\mathrm{mm}$.

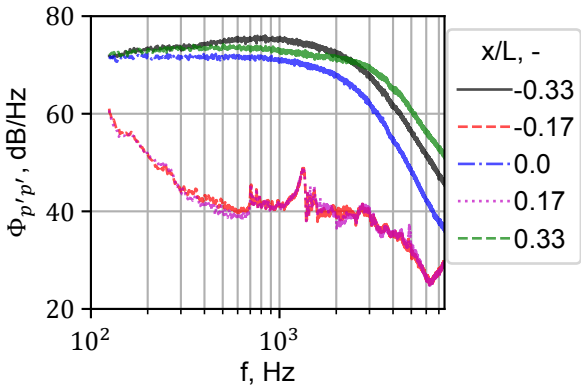

(c) Porous liner, $d_c = 4.5\,\mathrm{mm}$.

Figure 3: WPS measurements at $U_e = 20\,\mathrm{m\,s^{-1}}$, for one solid and the two porous DMND liners with cell size d_c.

Bibliography

[1] Tijdeman, H., "Investigation of the transonic flow around oscillating airfoils," Ph.D. thesis, Delft Technological University, Delft, The Netherlands, Dec. 1977. http://resolver.tudelft.nl/uuid:b07421b9-136d-494c-a161-b188e5ba1d0d.

[2] Choudhry, A., Arjomandi, M., and Kelso, R., "A study of long separation bubble on thick airfoils and its consequent effects," *International Journal of Heat and Fluid Flow*, Vol. 52, 2015, pp. 84–96. https://doi.org/10.1016/j.ijheatfluidflow.2014.12.001.

[3] Stark, R. H., and Genin, C., *Scaling Effects on Side Load Generation in Subscale Rocket Nozzles*, 2016. https://doi.org/10.2514/6.2016-4669.

[4] Ali, S. A. S., Azarpeyvand, M., and da Silva, C. R. I., "Trailing-edge flow and noise control using porous treatments," *Journal of Fluid Mechanics*, Vol. 850, 2018, pp. 83–119. https://doi.org/10.1017/jfm.2018.430.

[5] Salze, E., Bailly, C., Marsden, O., Jondeau, E., and Juve, D., *An experimental characterisation of wall pressure wavevector-frequency spectra in the presence of pressure gradients*, 2014. https://doi.org/10.2514/6.2014-2909.

[6] Curle, N., "The influence of solid boundaries upon aerodynamic sound," *Proceedings of the Royal Society of London A*, Vol. 231, No. 1187, 1955, pp. 505–514. https://doi.org/10.1098/rspa.1955.0191.

[7] Amiet, R. K., "Noise due to turbulent flow past a trailing edge," *Journal of Sound and Vibration*, Vol. 47, No. 3, 1976, pp. 387–393. https://doi.org/https://doi.org/10.1016/0022-460X(76)90948-2.

[8] Corcos, G. M., "Resolution of Pressure in Turbulence," *Journal of the Acoustical Society of America*, Vol. 35, No. 2, 1963, pp. 192–199. https://doi.org/10.1121/1.1918431.

[9] Bergh, H., and Tijdeman, H., "Theoretical and experimental results for the dynamic response of pressure measuring systems," Tech. Rep. NLR-TR F. 238, National Aerospace Laboratory NLR, Amsterdam, The Netherlands, Jan. 1965. http://resolver.tudelft.nl/uuid:e88af84e-120f-4c27-8123-3225c2acd4ad.

[10] Whitmore, S. A., "Frequency response model for branched pneumatic sensing systems," *Journal of Aircraft*, Vol. 43, No. 6, 2006, pp. 1845–1853. https://doi.org/10.2514/1.20759.

[11] Tijdeman, H., and Bergh, H., "The influence of the main flow on the transfer function of tube-transducer systems used for unsteady pressure measurements," Tech. Rep. NLR MP 72023 U, National Aerospace Laboratory NLR, Amsterdam, The Netherlands, Sep. 1972. http://resolver.tudelft.nl/uuid:3d3e7e72-7949-4d1a-8043-3194c42edff5.

[12] Bynum, D. S., Ledford, R. L., and Smotherman, W. E., "Wind tunnel pressure measuring techniques," Tech. Rep. AGARD-AG-145, North Atlantic Treaty Organization, Advisory Group for Aeronautical Research and Development, Nov. 1970. URL https://apps.dtic.mil/sti/citations/AD0714565.

[13] Samuelson, R. D., "Pneumatic instrumentation lines and their use in measuring rocket nozzle pressure," Tech. Rep. RN-DR-0124, Aerojet-General Corp., Sacramento, Calif. (USA), Jul. 1967. https://doi.org/10.2172/4212042.

[14] Van de Wyer, N., Zapata, A., Nogueira, D., and Schram, C., "Development of a test rig for the measurement of turbulent boundary layer wall pressure statistics," *2018 AIAA/CEAS Aeroacoustics Conference*, 2018. https://doi.org/10.2514/6.2018-3122.

[15] Pérennès, S., "[Aerodynamic noise sources characterization at low frequencies of high-lift devices] Caractérisation des sources de bruit aérodynamique à basses fréquences de dispositifs hypersustentateurs," Ph.D. thesis, École Centrale de Lyon, 1999. URL http://www.theses.fr/1999ECDL0032.

[16] Skilling, J., *Classic Maximum Entropy*, Springer Netherlands, Dordrecht, 1989, pp. 45–52. https://doi.org/10.1007/978-94-015-7860-8_3.

[17] Pereira, A., Antoni, J., and Leclère, Q., "Empirical Bayesian regularization of the inverse acoustic problem," *Applied Acoustics*, Vol. 97, 2015, pp. 11–29. https://doi.org/https://doi.org/10.1016/j.apacoust.2015.03.008.

[18] Azijli, I., Sciacchitano, A., Ragni, D., Palha, A., and Dwight, R. P., "A posteriori uncertainty quantification of PIV-based pressure data," *Experiments in Fluids*, Vol. 57, No. 72, 2016. https://doi.org/10.1007/s00348-016-2159-z.

[19] Goody, M., "Empirical Spectral Model of Surface Pressure Fluctuations," *AIAA Journal*, Vol. 42, No. 9, 2004, pp. 1788–1794. https://doi.org/10.2514/1.9433.

[20] Taback, I., "The Response of Pressure Measuring Systems to Oscillating Pressures," Tech. Rep. NACA-TN-1819, NACA, Langley Aeronautical Laboratory, Langley Air Force Base, Va., Feb. 1949. https://digital.library.unt.edu/ark:/67531/metadc55128/.

[21] Iberall, A. S., "Attenuation of Oscillatory Pressures in Instrument Lines," *Transactions of the American Society of Mechanical Engineers*, Vol. 72, No. 5, 2022, pp. 689–695. https://doi.org/10.1115/1.4016800.

[22] Pierce, A. D., *Acoustics: An Introduction to Its Physical Principles and Applications*, 3rd ed., Springer Cham, Cham, Switzerland, 2019. https://doi.org/10.1007/978-3-030-11214-1.

[23] Whitmore, S. A., and Fox, B., "Improved accuracy, second-order response model for pressure sensing systems," *Journal of Aircraft*, Vol. 46, No. 2, 2009, pp. 491–500. https://doi.org/10.2514/1.36262.

[24] Zawodny, N. S., Liu, F., and Cattafesta, L., "Transfer matrix modeling of a recessed microphone for unsteady surface pressure measurements," *Applied Acoustics*, Vol. 117, 2017, pp. 185–190. https://doi.org/10.1016/j.apacoust.2016.10.013.

[25] Gumley, S. J., "A detailed design method for pneumatic tubing systems," *Journal of Wind Engineering and Industrial Aerodynamics*, Vol. 13, No. 1, 1983, pp. 441–452. https://doi.org/10.1016/0167-6105(83)90163-0.

[26] Tijdeman, H., "On the propagation of sound waves in cylindrical tubes," *Journal of Sound and Vibration*, Vol. 39, No. 1, 1975, pp. 1–33. https://doi.org/10.1016/S0022-460X(75)80206-9.

[27] Sivia, D., and Skilling, J., *Data Analysis: A Bayesian Tutorial*, Oxford science publications, Oxford University Press, 2006.

[28] Dekking, F. M., Kraaikamp, C., Lopuhaä, H. P., and Meester, L. E., *Conditional probability and independence*, Springer London, London, 2005, pp. 25–40. https://doi.org/10.1007/1-84628-168-7_3.

[29] van Ravenzwaaij, D., Cassey, P., and Brown, S. D., "A simple introduction to Markov Chain Monte–Carlo sampling," *Psychonomic Bulletin & Review*, Vol. 25, No. 25, 2018, p. 143–154. https://doi.org/10.3758/s13423-016-1015-8.

[30] Dekking, F. M., Kraaikamp, C., Lopuhaä, H. P., and Meester, L. E., *Exploratory data analysis: graphical summaries*, Springer London, London, 2005, Chap. 15, pp. 207–230. https://doi.org/10.1007/1-84628-168-7_15.

[31] Smol'Yakov, A. V., "A new model for the cross spectrum and wavenumber-frequency spectrum of turbulent pressure fluctuations in a boundary layer," *Acoustical Physics*, Vol. 52, No. 3, 2006, pp. 331–337. https://doi.org/10.1134/S1063771006030146.

[32] Kanevče, G., and Oka, S., "Correcting hot-wire readings for influence of fluid temperature variations," *DISA Inf.*, Vol. 15, 1973, pp. 21–24. URL https://cir.nii.ac.jp/crid/1572543025369446528.

[33] Zamponi, R., "Investigation of turbulence-surface interaction noise mechanisms and their reduction using porous materials," Ph.D. thesis, Technische Universiteit Delft and von Karman Institute for Fluid Dynamics, Waterloosesteenweg 72, 1640 Sint-Genesius-Rode, April 2021. https://doi.org/10.4233/uuid:d332c7e3-87be-4ed6-aa71-e629ef77e07a.

[34] Bendat, J., and Piersol, A., *Random Data: Analysis and Measurement Procedures*, Wiley Series in Probability and Statistics, Wiley, 2011.

[35] Haario, H., Laine, M., Mira, A., and Saksman, E., "DRAM: Efficient adaptive MCMC," *Statistics and Computing*, Vol. 16, No. 4, 2006, pp. 339–354. https://doi.org/10.1007/s11222-006-9438-0.

[36] Shahmoradi, A., Bagheri, F., and Osborne, J. A., "Fast fully-reproducible serial/parallel Monte Carlo and MCMC simulations and visualizations via ParaMonte::Python library," *arXiv e-prints*, 2020, arXiv:2010.00724. URL https://ui.adsabs.harvard.edu/abs/2020arXiv201000724S.

[37] Basten, T. G. H., and de Bree, H.-E., "Full bandwidth calibration procedure for acoustic probes containing a pressure and particle velocity sensor," *The Journal of the Acoustical Society of America*, Vol. 127, No. 1, 2010, pp. 264–270. https://doi.org/10.1121/1.3268608.